MATERIAL PHASE DETECTION USING CAPACITANCE TOMOGRAPHY

Quinton Smit

Supervisor : Prof J Tapson

Department of Electrical Engineering

University of Cape Town

A dissertation submitted to the University of Cape Town in partial fulfilment of the requirements of the degree of Master of Science (MSc) in Electrical Engineering, Cape Town - April 2000.

OBJECTIVE

The aim of this research is to investigate the sensing capabilities of a self-tuning synchronous detection capacitance circuit when applied to a tomography system. This research has been carried out to provide engineers with evidence that the circuitry designed can effectively detect multi-phase mixtures in static tomography systems. The report covers various sensing methods used in capacitive tomography, cross-correlation techniques, and the application of neural networks for discrimination between the material phases. Image reconstruction techniques are not discussed in detail.

Capacitance methods are suitable for measuring two-component pipeline flows with different dielectric constants, such as water/oil, gas/oil, and solids/gas mixtures. A technique known as synchronous detection has previously shown to be a suitable method for capacitance and conductance measurement.

In this work we describe the application of such a capacitance/conductance measuring system to a material phase detection tomography system. The design and implementation of a static vessel used to perform all the experiments is discussed, as well as the method used to obtain the resultant capacitance measurements between the sensing electrodes. In addition, the multiplexing method used to obtain the 28 independent measurements is discussed, including the A/D conversion process, RS-232 interfacing, and mathematical manipulation of the data with the use of Matlab. Recommendations are made on how the data can be used to effectively distinguish between the various material phases by means of mathematical image reconstruction. Results have proved that we are able to distinguish between the three primary phases, water, air, and rock.

This study therefore proves that there is sufficient grounds for the further development of a dynamic tomography system using the synchronous detection method of capacitance sensing.

ABSTRACT

The design of sensor electronics for a tomographic imaging system based on electrical capacitance sensors is of interest in many different engineering applications. This can be especially beneficial in industrial two-component flow systems where capacitance tomography may provide information on how the two components are distributed, and the overall mass flow rate.

Conventional flowmeters are often unsuitable for accurate measurements in two phase flows. This is particularly prevalent in cases where the component distribution is varying in space and time. Computerised tomographic methods used in medical imaging, can provide a useful means for obtaining almost instantaneous information on the distribution of components in a cross section of a pipe. This aspect is exploited in this work leading to the possibility of a more accurate and relevant measurement. Several different flow imaging techniques have been developed based on neutron, x-ray, capacitance and ultrasound techniques.

This work firstly reviews the recent developments in tomographic systems with particular reference to measurements in industrial processes. The principle flow sensing methods are summarized including cross correlation techniques and their applications. Application methods of artificial intelligence for image reconstruction are also reviewed as these techniques will be required in future developments.

Secondly, the aim of this study has been to design and construct a static capacitance tomography system. An existing circuit, used to measure capacitance and conductance by means of synchronous detection was modified and applied to a simulated multi-phase flow test-bed system. It is well-known that a measurant's capacitance is proportional to its dielectric constant and the dielectric constant of water, rock and air are all different. A static measuring system was constructed consisting of eight capacitive sensing electrodes and an outer grounded plate to minimise the effects of stray capacitance. By multiplexing the sensing electrodes through reed

relays to the synchronous detection capacitance circuitry, all 28 sensing combinations could be implemented. These resultant output voltages representing the capacitance measured between each of the 28 sensing electrodes are converted into a digital format by means of an A/D and micro-controller.

Experimental results revealed that our system was able to produce repeated results that indicated a divergence in capacitance sensor output voltages when measuring various combinations of rock, water, and air. The industrial goal was to prove that our system could detect the difference in material phases. To determine the differentiation, a simple approach using a graphical transformation, and an interpolation into a three dimensional contour/surface graph was used. This is in essence a front end to which artificial intelligence in the form of neural networks can be implemented to effectively distinguish between the various phases.

This work has resulted in the following publications:

International Conference Presentations:

1. Q Smit, B Mortimer, J Tapson, "General Purpose Self-tuning Capacitance Sensor", IEEE, Instrumentation and Measurement Technology Conference (IMTC), St Paul, Minnesota, USA, May 1998.
2. Q Smit, J Tapson, B Mortimer, "Development of a Material Phase Detection System using Capacitance Tomography", IEEE, Africon'99 Conference, Cape Town, South Africa, September 1999.

This thesis is dedicated to my wife
Karén and my daughter Suné
for all their support and love

ACKNOWLEDGEMENTS

The author would like to thank Prof. J. Tapson for his excellent supportive and inspirational supervision, as well as his willingness to share his profound knowledge with others. Prof B. Mortimer is acknowledged for his advice and explanation of the various capacitive sensing techniques. The financial support from DebTech and the NRF is gratefully acknowledged. Mr J.D. Human is thanked for the manufacturing of the printed circuit boards. Many thanks to all staff and students at The Centre for Instrumentation Research, Department of Electrical Engineering, Cape Technikon who all contributed to an enjoyable working environment.

TABLE OF CONTENTS

CHAPTER 1 :

INTRODUCTION

New generation electrical capacitance tomography systems using an AC-based capacitance measuring circuitry have been developed by UMIST [1]. These systems have improved signal-to-noise ratios by a factor of 10 compared to other existing systems, and can measure capacitance down to 0.1 femtoFarads. The aim of this thesis is not to compete with these efforts, but to develop a system that would be cost effective and reliable for our specific application.

This chapter introduces recent developments in the design and application of tomographic sensors for measurements in industrial processes. The principal sensing methods and their relative performance together with the applications, limitations and future developments are discussed.

1.1 Background to Process Tomography

Process tomography is used to improve the operation and design of systems handling multi-component mixtures, by imaging these components in real-time with the use of non-intrusive sensors. From these images it is possible to determine how the internal flows, component concentrations and flow rates are behaving. There is a widespread need for the direct analysis of the internal characteristics of process equipment by means of non-invasive, robust sensors situated at inaccessible locations. Using capacitance tomography in industrial applications allows more detailed monitoring of processes and therefore more complex control of process equipment.

The tomographic field evolved essentially during the mid 1980s when work started at the University of Manchester Institute of Science and Technology (UMIST) on electrical capacitance tomography for the imaging of multi-component flows from oil wells [1]. The capacitance transducers used were only suitable for electrically non-conducting applications [1]. The potential use of electrical impedance tomography (EIT) as a safe, low-cost method for imaging the human body was also realised during this period [1]. In 1988 work started at UMIST on the

development of EIT for imaging vessels containing electrically conducting fluids. With the use of medical EIT, the location of objects in space was made possible. Further work in microwave imaging undertaken by Beck and Plaskowski [2] resulted in the measure of both location and velocity of movement.

With the development of low-cost processors during the 1980s the problem of image reconstruction has improved tremendously, resulting in process tomography becoming a cost-effective technique. Developments in the availability of sophisticated computer aids provide the design engineer with the ability to design systems with a variety of modelling techniques. Together with the sensing methods of process tomography, model verification in an industrial environment is realised.

1.2 Principles of Capacitance Tomography

By measuring the dielectric properties of a material inside a vessel, the distribution of the contents can be determined. Typical information obtainable can include cross-sectional images of the vessel contents, the measurement of the volume fraction of different constituents (or phases), and the velocities of the contents in multi-phase flows. The basic capacitance tomography system, shown in Figure 1, will consist of a capacitance sensor, a capacitance measuring unit, and a control computer.

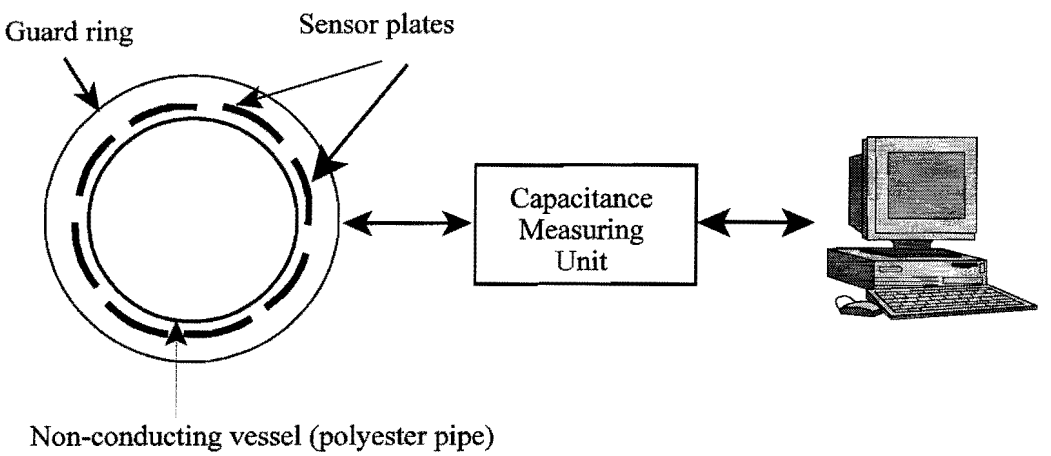

Figure 1: A schematic representation of a basic capacitance tomography system, consisting of a pipe surrounded circumferentially by capacitance plates, a measuring unit, and a computer.

The cross-section to be imaged is surrounded circumferentially by one or more sets of capacitance electrodes, and the electrical capacitances between all combinations of the electrodes within each set are measured. This information is then used to construct an image of the contents of the cross section of the vessel enclosed by the sensor, based on the permittivity of the material inside the vessel. If two or more sets of electrodes are fitted to the pipe and spaced a short distance apart, it is possible to measure axial flow velocity of the material inside the pipe by correlating information from the two sets of capacitance measurements.

1.3 Methods used in Capacitance Tomography

In many of the tomographic systems developed the number of electrodes mounted around the measurement volume differ. The system described by He *et al* [3-4] and Johansen *et al* [5] makes use of a six-electrode sensor, whereas Xie *et al* [6-8] and Huang *et al* [9-10] used eight-electrode systems.

The electrodes should be arranged around the boundary of the sensing region, and the capacitances between all the combination pairs measured. Generally, for an n-electrode sensor, the number of linearly independent combinations [*LIEC*] between these pairs are calculated from the formula below. For example, with a system that has $n = 8$ electrodes, the total number of linearly independent electrode combinations are:

$$\begin{aligned} LIEC &= \frac{n}{2}(n-1) \\ &= \frac{8}{2}(8-1) \\ &= 28\ LinearlyIndependantCombinations \end{aligned}$$

The resulting numbers of linearly independent electrode combinations for other sensor systems is given in the table below.

Linearly Independent Electrode Combinations (LIEC) Formula	16-electrode sensor (LIEC)	12-electrode sensor (LIEC)	8-electrode sensor (LIEC)
$\frac{n}{2}(n-1)$	120	66	28
$\frac{n}{2}(n-3)$	104	54	20
$\frac{n}{2}(n-5)$	88	42	12
$\frac{n}{2}(n-7)$	72	30	4
$\frac{n}{2}(n-9)$	56	18	-
$\frac{n}{2}(n-11)$	40	6	-
$\frac{n}{2}(n-13)$	24	-	-
$\frac{n}{2}(n-15)$	8	-	-

Table 1: The number of linearly independent electrode combinations for the selected sensor system is calculated with the formula shown in the left column.

The main problem encountered with a larger numbers of segments is the reduced signal level, and capacitive fringing. The shielding of the sensor in the axial direction is of crucial importance to avoid electromagnetic interference. The inclusion of a ring-electrode connected to earth potential acts as a strong sink for electromagnetic fields, as proposed by Reinecke and Mewes [11]. In addition to this the stray immunity of the circuit is very important to avoid extensive noise being introduced into the extremely small signals. Additionally the stray capacitance may vary with cable movement, ambient temperature changes, component variation, and external or internal electric field changes. The charge/discharge and AC-based circuits are the most suitable for the use in ECT systems because, in principle, they are stray-immune [12].

With this method Reinecke and Mewes [11] showed that the total number of linearly independent measurements can be improved, yielding a more detailed reconstruction. Klug and Mayinger [12] used a set of completely different electrode combinations in which the driving and measurement electrodes were distributed all around the measurement volume, increasing the linearly independent measurements even further. Huang and Plaskowski [13] also made use of this method where different sections on the cross-section of the fluid-conveying pipe were interrogated by measuring the capacitance of different electrode pairs in an eight-electrode system. The basic measuring circuit used is shown in Figure 2 (see Huang *et al* [9]).

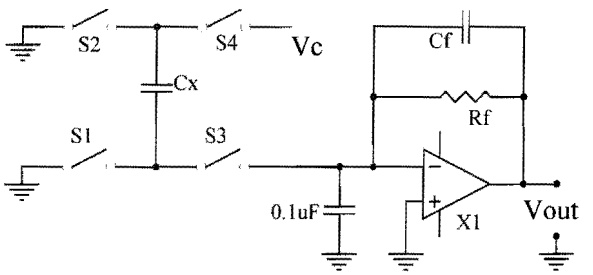

Figure 2: Capacitance measuring circuit, showing the CMOS switches that charge and discharge the pump capacitor C_x, and the operational amplifier X_1 producing the output voltage proportional to the capacitance value C_x.

One side of the capacitor C_x (known as the active electrode), is exposed to the supply potential or ground potential by the CMOS switches S_2 and S_4. The other side of the electrode known as the detecting electrode is connected to earth potential by switch S_1, or to the input of the current detector via S_3. The current detector averages the charging and discharging pulses flowing through the detecting electrode, producing a voltage signal, V_{out}, proportional to the unknown capacitance value C_x.

$$V_{out} = (KfV_c)C_x$$

where K is the gain factor of the current detector and f is the frequency of the charge/discharge operation.

In an 8-electrode tomography system, the capacitances between electrodes 1 and 2, then 1 and 3, and so on up to 1 and 8, are measured and fed to the data collection system. Next, electrode 2 is selected as the active electrode and pairs 2-3, 2-3, ..., 2-8 are measured. With this system a total of 28 independent measurements are made. In this measurement process Huang *et al* [8] ensured that the redundant electrodes were always connected to earth, forming 'guard rings' for the measuring electrodes. This arrangement enabled the measurement sensitivity to be focussed into a narrow area between the selected electrode pair. Experimental results showed that the image resolution was not high due to the number of independent measurements and the dimension of the electrodes. They found that increasing the number of electrodes to a 16-electrode system, produced 120 independent measurements, thereby improving the image quality. However, increasing the number of electrodes requires a more sensitive and stable measuring circuit in order to resolve even smaller capacitances. Huang *et al* found that in some industrial applications, a low-resolution image is often adequate to provide the information required to identify the flow regime.

Other similar capacitance transducer methods making use of the charge transfer principle have been developed by Fielden [14]. Huang *et al* [15] describes a new design of charge transfer transducer that has a low baseline drift, high sensitivity, and overcomes the stray effects experienced with parasitic capacitances. This method is illustrated in Figure 3.

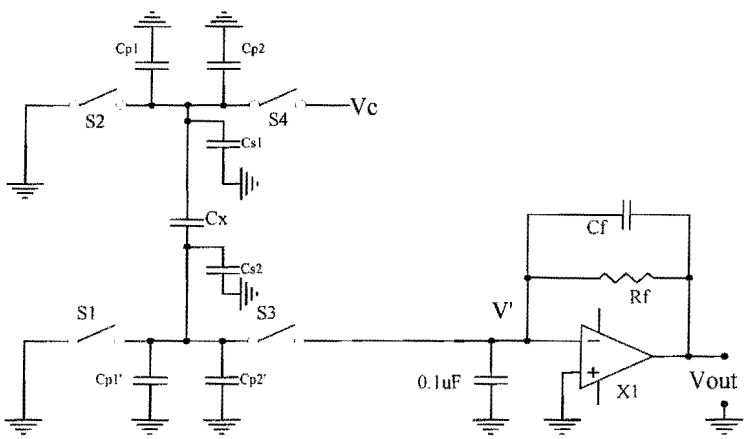

Figure 3: In this stray-immune circuit diagram, the capacitors connected in close proximity to the CMOS switches and detecting electrode, reduce the effects of stray capacitance.

To achieve a high stray-immunity, the potential of the detecting electrode should be kept at earth or virtual earth potential during the charge and discharge interval. It was found that the potential varied during various switching transients, firstly, due to the finite ON resistance (R_{on}) of the semiconductor switches at the switch-on moment, and secondly, the control signals to the gates of the switches (S1 and S2) produced voltage spikes at the output of the switch due to the intrinsic gate-source capacitance of the FET switch. The following measures were taken to overcome these effects:

- A capacitor is connected as near to the detecting electrode as possible to absorb the voltage spikes and smooth the charging and discharging current pulses. However, the maximum capacitor value is limited by the sampling frequency. In practical applications the value of the capacitance was determined by experimentation.
- To reduce the stray inductance of the connecting wire, the shortest practical length of coaxial cable should be used to connect the detecting electrode to the switches.

1.4 Principles of Electrical Resistance Tomography

Unlike electrical capacitance tomography systems, the sensors in electrical resistance tomography (ERT) must be in continuous electrical contact with the flow regime. In addition, the sensors must be more conductive than the measured material in order to achieve good results. In most cases the electrodes are metallic and can be manufactured from stainless steel, silver, gold, platinum, or any suitable material that provides good electrical conduction and resistance to abrasion and corrosion. The electrodes are placed in similar positions to the capacitance tomography systems, ensuring precisely defined intervals in order to achieve accurate image reconstruction. Dicken and Wang [16] found that the quantitative algorithm they used for image reconstruction is highly sensitive to electrode placement. The size of the electrodes is another important factor when using current-injecting ERT systems. A large surface area is required for current-injecting electrodes to ensure an even current density [17,18]. On the other hand, when using voltage measuring ERT systems, a small surface area is optimal to avoid 'averaging' several equipotentials. Typical examples of these compound electrode structures are described by Hua *et al* [18], and shown in Figure 4. In the compound structure, the current source is fed

to a large surface outer area, ensuring an even current density generated within the vessel. The voltage measurement is made via an insulated point-sized central electrode [16].

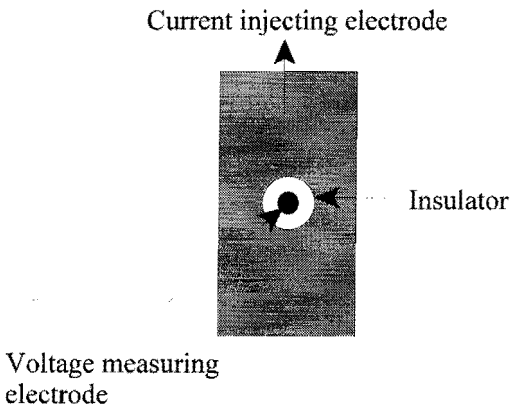

Figure 4: The current injecting electrode has a larger surface area, ensuring and even distribution inside the vessel, whereas the voltage measuring electrode is point-sized to avoid 'averaging' several equipotentials [19].

Wang *et al* [19] developed a series of analytical and numerical models to investigate the error due to employing larger electrodes for voltage measurement, and their conclusion, confirmed by Piheiro [40], was that the loss in measurement sensitivity as a result of using larger electrodes was minimal.

Various methods are employed to attach the metal electrodes to the walls of electrically conducting and non-conducting process vessels, as shown in Figure 5.

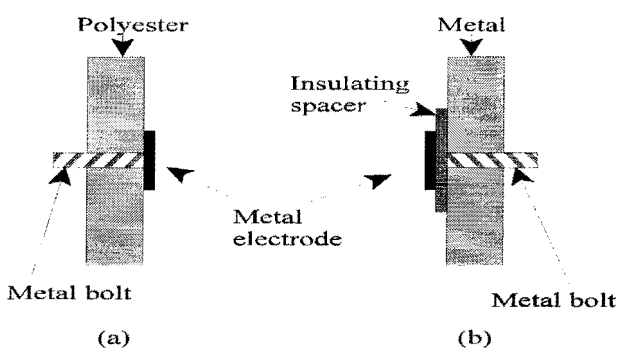

Figure 5: An electrode fitted onto an polyester or acrylic wall, as in (a), need not be insulated from the wall of the vessel by means of an insulating spacer [19].

Figures 5(a) and (b) show the cross section of a metal electrode attached to a polyester and metal-walled vessel respectively. An insulating spacer is inserted between the wall of the vessel and the electrode in the metal-walled vessel, with the dimensions of the spacer being wider and taller than the metal electrode [16]. For both the conducting and non-conducting walled vessels, holes were drilled into the vessel to mount the electrodes [16].

Dickin and Wang [16] also noted that the length of the signal-carrying cable between the electrode and the current injection/voltage measurement circuitry was critical. They found that the longer the cable, the larger the associated stray capacitance and leakage current, resulting in undesirable phase-shifted signals. Heavy duty machines are a source of electromagnetic radiation prevalent in process environments, resulting in these unwanted signals being induced into the cabling.

Depending on the requirements of the process application, robust electrical resistance tomography systems can be relatively cheap to construct.

CHAPTER 2:

AC BASED "LOCK-IN DETECTION" TECHNIQUE

2.1 Background

In previous research by Tanner [20], the AC based "lock-in detection" circuit developed by Marioli *et al* [21] was used to develop an simple benchtop instrument which could provide a quick and accurate measurement of the percentage of water in an oil sample. Tanner successfully developed an instrument to make real-time on-line assessments of both the capacitance and conductive loss of a liquid stream independent of one another, as it passes through a sensor. Experimental results by Tanner revealed a linear relationship between the output of the instrument's capacitive sensing element and the measured oil sample's water content, suggesting that this instrument is suitable for the assessment of the water content of recycled oil [20].

The method used was nonetheless affected by frequency and phase drift due to external factors, resulting in the basic circuitry being further improved with the introduction of a self-tuning feature developed by the present author [22]. With the successful introduction of digitally controlled potentiometers in the phase controlling circuitry, the author [22] proved that the self-tuning capabilities of a synchronous detection based capacitance measuring instrument provided the solution to the tuning and stability problems experienced by the standard technique. Experimental results again showed a high degree of linearity for both the self-tuning instrument's capacitive and loss conductance sensing element, over a large range of capacitance and conductance values respectively. Results also showed that the instrument repeated the same measurement over a period of time even after the power was removed and then restored. In addition, the PIC micro-controller controlling the Dallas digital potentiometers was an effective method of ensuring that the phase shifted frequencies were kept stable. This ensured that synchronous detection which is dependent on a stable and accurate phase shifted frequency could function correctly [22].

2.2 AC Based "Lock-in Detection" Technique with Multiple Feedback

A functional block diagram of the measurement technique is presented in Figure 6.

To improve on the AC based "lock-in detection" technique, we have introduced multiple feedback loops based on the measurement technique of Marioli *et al* [21].

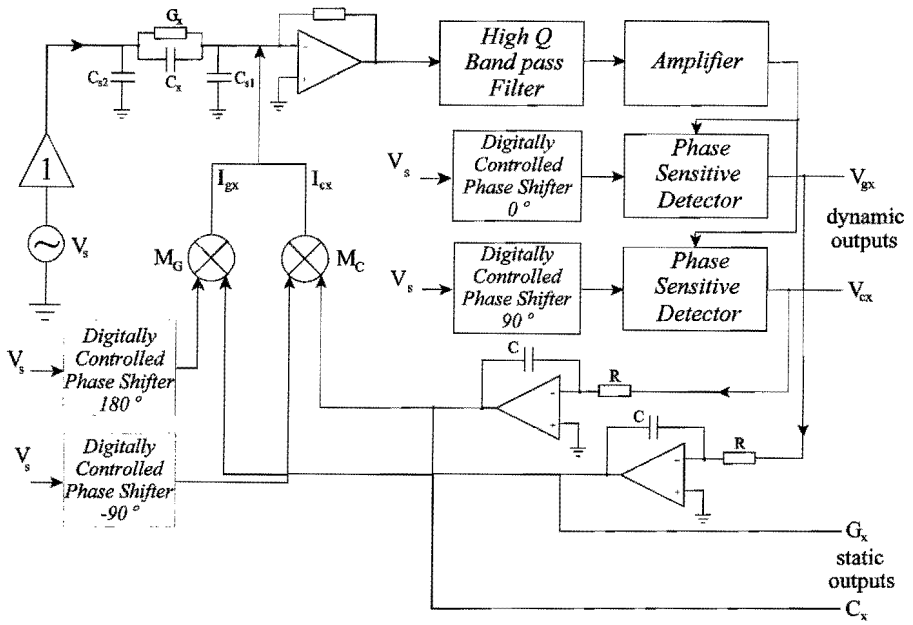

Figure 6: The original circuit developed by Marioli *et al* [21] employing an auto-balancing technique via negative feedback is shown, including the newly designed digitally controlled phase shifting circuitry.

The operation of the circuit can be summarised as follows: the sensor capacitor is driven by a sinusoidal signal V_s, which is frequency stabilized and frequency controlled. The current through the capacitive sensor consists of an in-phase and quadrature component with amplitudes related to the measured loss conductance G_x and capacitance C_x between the sensor electrodes, where G_x and C_x are the conductance and capacitance of the sample. The vector sum of these components is converted to a voltage signal by means of a current to voltage amplifier. Each of these output voltages are synchronously demodulated or detected by a quadrature phase sensitive detector. This is now passed through a low-pass filter which rejects the AC components and produces resultant DC voltages V_{cx} and V_{gx}, whose amplitudes are proportional to C_x and G_x respectively. These two signals are integrated and multiplied with carrier signals in opposite phases with currents passing through C_x and G_x. The outputs of the two multipliers are converted into

currents which in turn subtract from those passing through the sensor. Effectively, the current due to the mean values of the sensor capacitance and loss conductance is cancelled by these subtracting currents I_{cx} and I_{gx}, controlled by means of two separate feedback loops. The magnitudes of the capacitance and loss conductance are measured in terms of the current required to cancel them. The output signals are taken from the outputs of the integrator stages to produce DC outputs as a function of C_x and G_x respectively.

2.3 AC Based "Lock-in Detection" Technique with Multiple Feedback Circuit Stability

The stability of the carrier frequencies are of great importance to the overall accuracy and stability of the "lock-in detection" method. Marioli *et al* [21] and Tanner [20] failed to address this important aspect and found that their instruments could not maintain long term stability and accuracy with temperature drift. Industrial noise and stray capacitance also affected the accuracy of the system. In our work we have developed the self-tuned circuit to address the problems experienced with instability and accuracy. Practical problems in the implementation of the original circuit were the internal phase shifts of the components caused by temperature and other external influences. Using equal arrangements of similar components in each signal path meant that the phase shift was approximately the same. However, "tuning" of the system was complex and still subject to "drift".

2.4 Self-Tuning AC Based "Lock-in Detection" Technique Implementation

A method to firstly detect the phase between two signals (reference and phase shift), and a technique to vary the phase shift were required. A prototype self adjusting phase shifting circuit using digital potentiometers and a PIC micro-controller was implemented. The digital potentiometers controlled the phase shift in response to the PIC micro-controller. The PIC micro-controller was used to measure both the phase shift and control the system. The electronic implementation of the self-tuning AC based "lock-in detection" method is discussed in further detail below.

2.4.1 The Signal Source

The signal source has been constructed using a XR2206 IC oscillator. The selected sensor capacitor is driven by a 60 kHz, 4V peak sinusoidal signal which is frequency stabilised and amplitude controlled. However, the signal source as constructed is capable of being operated within a range of frequencies from 30 kHz to 80 kHz; the signal amplitude is also variable.

2.4.2 The Phase Sensitive Detector/Demodulator

The phase sensitive demodulator was constructed using an AD633 four quadrant analog multiplier IC. The signal on the output of the current detector is multiplied with an appropriately phase-shifted sinusoidal reference signal, thus producing an AC signal double the original signal frequency, plus a DC component. The first-order low pass filter of the demodulator effectively filters out the AC component passing only the DC signal.

2.4.3 The Integrator and Modulator in Feedback Loop

An integrator was realised using a LF356 operational amplifier and appears in the feedback path of the circuit. The modulator has been constructed using an AD633 four quadrant analog multiplier. The DC signal on the output of the integrator is multiplied with an appropriately stable phase-shifted sinusoidal signal (carrier) and converted to a equivalent current which is equal in magnitude, but opposite in phase to the signal passing through the sensor. Part of the original instability is due to the variation of these reference phases caused by component variation. It should be noted that this implementation of the circuit maintained the correct phase-shifted sinusoidal signal (carrier) due to the digital potentiometers and PIC micro-controller which is described in the next two sections.

2.4.4 The Phase Shifters

Large signal phase shifts from approximately 0° to 180° have been achieved with the circuit shown in Figure 7. The output phase of the signal can be varied manually without any variation in the signal magnitude.

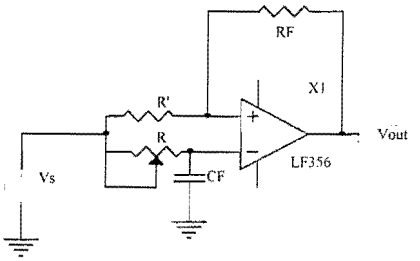

Figure 7: The basic phase-shifting circuit with the potentiometer R to adjust the phase of the input frequency from 0° - 180°, is shown. The value of CF is chosen around the input frequency, and the gain resistors R' and RF are selected for a gain of 1.

However, in order to ensure that the circuit maintains the accuracy and stability levels required for the complete system, constant re-adjustment of the phase shifters is needed. To accomplish this in our initial system, individual printed circuit boards had to be removed, adjusted, and re-inserted to tune the circuit. The phase was adjusted using 10-turn potentiometers. Since there are multiple feedback paths, different phase shifts are required for the implementation of the synchronous detection paths. Components used in the structure of the circuit are susceptible to temperature drift and noise. Re-adjustment of the phase frequencies is a time consuming task involving the removal and re-calibration of parts of the circuit in the laboratory. Our aim was to remove the manual phase tuning of the instrument (adjusting of the 10-turn potentiometers) and to automate this process. Self-tuning of the phase shifted frequencies was also required, and would also have to be performed while the circuit is in operation. It is apparent that a micro-controller was needed to control the system.

The PIC 16C73 micro-controller was found to be well suited for our application. Some of the 16C73 peripheral features included:

- 33 I/O pins with individual direction control.
- Two pins that could be configured as capture input, PWM output, or compare output. The capture input, which was used to capture the 60Khz signal needed to measure the phase of the signal, is a 16-bit register with a maximum resolution of 200ns.
- Serial communications interface for full duplex asynchronous or half duplex synchronous communications.

2.4.5 The Digital Potentiometers

By replacing the preset potentiometer (R in Figure 7), with a DS1804 non-volatile digital potentiometer, the phase angle of the incoming frequency could be adjusted using digital control rather than manual adjustment. In this system the phase could automatically be adjusted from 0 to 180 degrees. The device provides an ideal method for low-cost trimming applications using a micro-controller with minimal external circuitry. Wiper position of the DS1804 can be stored in EEPROM memory on demand. The device's wiper position is manipulated by a 3-terminal port that provides an increment/decrement counter controlled interface.

The DS1804 is available in three resistor grades which include the 10 kΩ value used in our application, a 50 kΩ value, and a 100 kΩ value. The software written for the micro-controller operation include features for storing the wiper position. On power-up, the DS1804 loads the value of EEPROM memory into its wiper position register. The value of this register can then be set to another wiper position if desired, by using the 3-terminal control port. On power-up, the wiper position will be loaded within 500 μs once the power-supply is stable. Additionally, the 3-terminal interface port is active after 50ms. Software routines are required to ensure that on the next power-up, the value of the EEPROM memory is loaded into the wiper position register. The DS1804 is specified to accept 50,000 writes to EEPROM before wear-out condition. After wear-out the DS1804 will still function and the wiper-position can be changed during powered conditions using the 3-terminal control port. However, on power-up the wiper-

position will be indeterminate. For our application, four DS1804 digital potentiometers were used in 4 phase shifters to perform the reference phase shifts required for multiple feedback lock-in detection.

2.5 Frequency Control

In Figure 8 it is shown that the PIC16C73 micro-controller performs the following functions:

- To compare the phase shifted signal to the phase of the 60 KHz signal.
- To adjust the DS1804 digital potentiometer UP/Down pin, until the correct phase shift has been achieved.

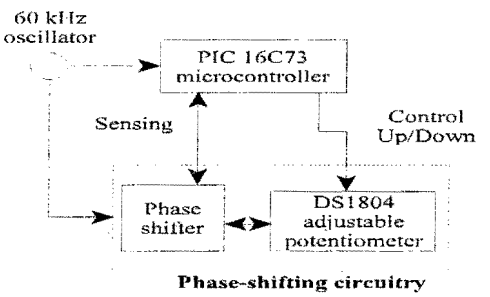

Figure 8: The 60 kHz oscillator reference frequency is fed to the phase-shifting circuitry and the 16C73 micro-controller respectively. The 16C73 micro-controller compares the phase of the reference 60 kHz signal to the adjusted signal via the sensing input, and adjusts the DS1804 potentiometer Up/Down, via the control output until they are equivalent.

Switching the stable 60 kHz signal from the oscillator to the port pin of the micro-controller is performed by MAX4547 low voltage bi-directional RF switches. The MAX4547 is a low-voltage T-switch designed for switching RF and video signals from DC to 300 MHz in 50 Ω and 75 Ω systems. The MAX4547 contains two single-pole/double-throw (SPDT) switches. Each switch is constructed in a "T" configuration, ensuring excellent high-frequency off-isolation and crosstalk of -80dB at 10 MHz. The on-resistance is 20 Ω and the off-leakage current is less than 5 nA at +25 °C and 50 nA at +85 °C. This makes the MAX4547 an ideal choice for our application as it consumes low power and

switches at the required frequencies. By converting the sinusoidal waveform from the oscillator to a square wave of equal frequency and duty cycle, the 16C73 micro-controller in Figure 9 is able to work with definite rising and falling edges. These 60 kHz square wave pulses are now also equivalent to TTL logic levels of 0V and +5V. The square wave oscillator signal is now switched to the internal micro-controller counter by means of the MAX 4547 RF switches. The internal counter will start running as soon as the rising edge of the 60 kHz pulse is received. After the rising edge has been detected by the micro-controller, the controller disconnects the stable 60 kHz square wave signal, and switches in the phase-shifted 60 kHz square wave.

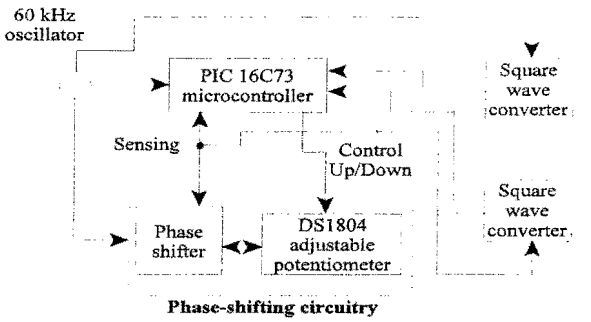

Figure 9: The 60 kHz oscillator reference signal is converted to a square wave signal. This is compared to the phase-shifted signal that is also converted to a square wave, and constantly controlled to the correct phase by means of the phase shifter and DS1804 digital potentiometers.

The counter is stopped as soon as the rising edge of this waveform is detected. The phase shift of the signal can be accurately be determined by making use of simple mathematical software routines. Four different phase shifts are required for the individual stages of the lock-in detection measurement technique of Marioli *et al* [21] to function correctly, namely; 0°, 90°, -90°, and -180°. These four phase shifted signals have to remain at the correct phase shift for the circuit to be accurate and stable, but must also compensate for the internal phase shifts of the components in the circuit path. The 16C73 micro-controller used to perform the operation has to measure four individual phase shifted signals, compare this to the stable oscillator frequency, adjust the DS1804 digital potentiometers to maintain the correct phase shift as well as allow the dielectric measurements to take place. Alternative CMOS DG300 analog switches were used to switch the signals to the micro-controller, but were found to be to costly compared to the MAX4547. Thus the time-consuming task of setting the resistances has been avoided using this technique: a significant improvement

over the original multiple feedback lock-in detection technique.

2.6 The Multiplexer Circuitry

Two MAX350 multiplexer ICs driving reed relays, shown in Figure 10, were used in conjunction with the 16C73 micro-controller to form the multiplexer circuitry. In order to achieve the 28 independent measurements from the sensing electrodes, we decided to use one MAX350 multiplexer to drive the master sensing electrode and the other to switch between the receiving electrodes. These multiplexer ICs were used to drive the sensing electrodes, but it was discovered that the on-resistance and on-capacitance of the MAX350 ICs affected the readings obtained. With the introduction of reed relays, this problem was overcome. The reed relay contacts switches the capacitance electrodes on the tomography rig to the synchronous detection circuitry where the signals are converted to voltages. The final voltage signal each of the 28 combinations of capacitive sensing electrode elements were taken from the output of the integrator stage to produce a static (DC) output voltage, as a function of the mean capacitance. This resultant output voltage measurement is converted to its digital equivalent by means of the PIC16C73, 8-bit analog-to-digital (A/D) converter. The digital equivalent is transmitted to the PC via a 9600 baud, RS-232 link. Here, the data is gathered for further manipulation for graphical display.

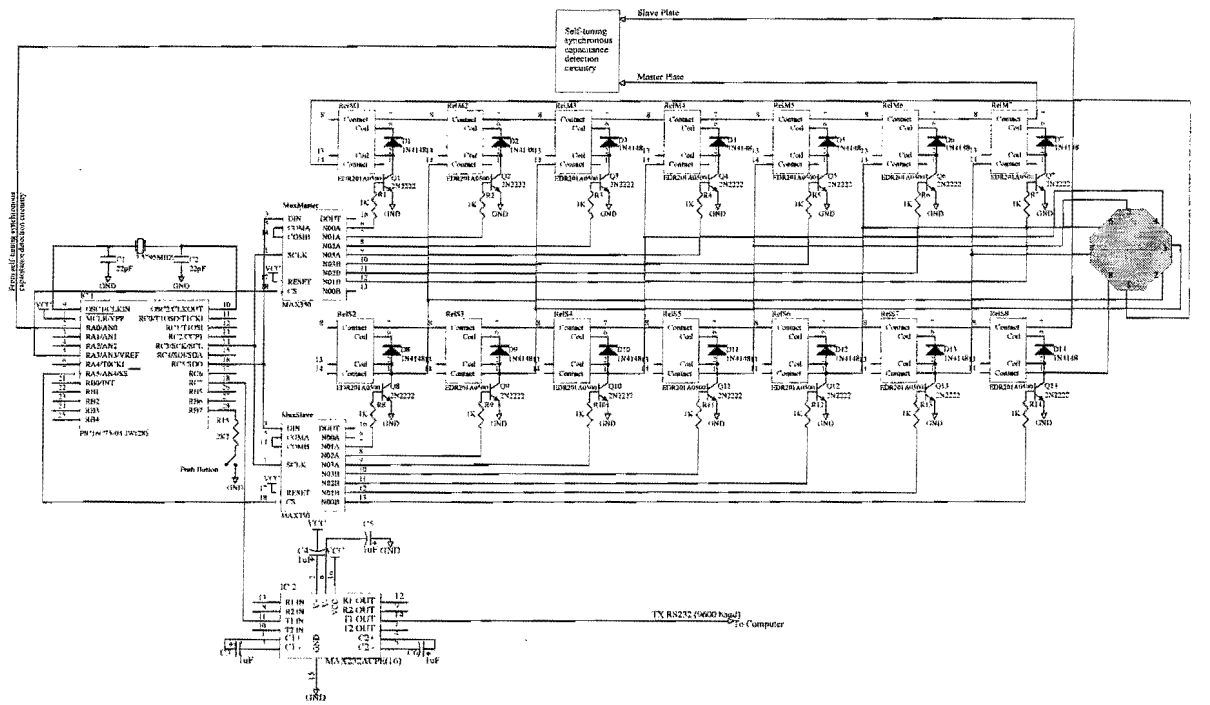

Figure 10: The PIC16C73 micro-controller, on the left, regulates all the various actions in the process. The multiplexer and reed relays switch the 28 capacitance electrode combinations to the PIC16C73 analog-to-digital converter. The resultant 8-bit digital equivalent of the output voltage, a function of the mean capacitance between electrodes, is transmitted to the PC via a RS-232 link.

CHAPTER 3 :

CROSS CORRELATION FLOWMETERS

The measurement of plant parameters is essential for the complex control and management of industries. Flow measurement is a particularly important aspect of plant instrumentation, with well established techniques available for the measurement of clean single-phase fluids. Cross correlation flowmeters are ideally suited for the measurement of multi-phase flows and also to the problem of obtaining reliable measurements at inaccessible locations. The basic principle of cross correlation flowmetering is to measure the time taken by a disturbance to pass between two known points along the direction of flow. Beck and Plaskowski have researched the scientific and design features of cross correlation flowmetering, and presented their results with a practical industrial problem-solving approach [23].

3.1 The Development of Cross Correlation Methods for Flow Measurement

The concept of flow measurement based on measuring the transit time of some disturbance between two points was first published by Kozubowski (24) and Balachandran (25), with the first description of a cross correlation application given by Komiya (26). A paper by Battye (27) on an application not involving flow measurement (steel strip velocity measurement) did much to increase the awareness of cross correlation for measurement. Recording the natural disturbances occurring in the flow medium was found to be more practical than injecting disturbances for cross correlation flow measurement. The earliest full explanation of the use of natural disturbances in cross correlation flow measurement was given by Beck and Plaskowski [23]. This work was patented by these authors and led to a major programme of work in the School of Control Engineering, University of Bradford, England, and later in the Department of Instrumentation and Analytical Science, University of Manchester Institute of Science and Technology [UMIST], England.

Ultrasound transducers, being inherently non-contacting, were regarded as attractive for cross correlation flow measurement and Coulthard's work [28] was extended by Wormald *et al* [29],

who designed ultrasonic systems suitable for use in large-diameter pipes. Ong [30] further extended the use of ultrasonic transducers to the measurement of the flow of a range of liquids and slurries in pipes. The disadvantage of ultrasonic systems was the continuous manual re-adjustment of the transmitted frequency to obtain satisfactory cross correlation. Battye [27] invented an ingenious closed-loop system to maintain tight phase control automatically, thereby producing an industrially acceptable instrument. The success of the closed loop systems led to their evaluation as 'clip-on' systems working through the wall of the pipe.

With the setting up of the new Department of Instrumentation and Analytical Science at UMIST in 1980, the problem of three-component flow measurement in oil/gas/water mixtures was investigated by Hammer [31], who described a system using capacitance transducers to measure the flow of all three components. Impedance measurement systems were also developed by Dykesteen *et al* [32], with methods for measuring the velocity of each component in a multi-component flow being developed by Xu *et al* [33].

In 1985 the group at UMIST examined the industrial requirements for multi-component flow. In many cases the spatial distribution of the components was unknown and variable, thus reducing the accuracy when measuring spatial distributions of measured components that are not uniform. This led to an intense programme of work on 'flow imaging' which involves using a number of sensing transducers around a pipe and image reconstruction software to provide accurate information for flow measurement.

Many early industrial applications of cross correlation techniques were in the nuclear industry where it is important to measure the flow in tubes in a nuclear reactor to prevent 'flow starvation' that could lead to 'hot spots' and consequent danger. Over the years the nuclear industry continued to develop cross correlation flowmeters for a variety of applications. A method of measuring the coolant flow using transit time analysis of nitrogen isotopes is described in publications by the Research Institute for Physics, Hungary [34].

3.2 Basic Principles of Random Data Analysis, As Applied to Pipeline Flow

The following discussion on random data analysis for cross correlation flowmeters, covers the theory behind transit time analysis of random signals, as found in the study by M S Beck and A Plaskowski [35]. The cross correlation method of flow measurement is based on the determination of the transit time of a measurable disturbance moving along the pipe over an exactly known distance. The time delay of the maximum value of the cross correlation function gives an indication of the transit time between the transducers, from which the actual flow measurement is obtained.

Random processes such as the turbulence phenomenon in pipe flows cannot be described by a mathematical relationship because each observation of the phenomenon will be unique and will represent only one of the many results which might have occurred, as shown in Figure 11. A single time history representing a random phenomenon is called a sample function when observed over a infinite time interval [35]. The collection of all possible sample functions that the random phenomenon might have produced is called a random or stochastic process.

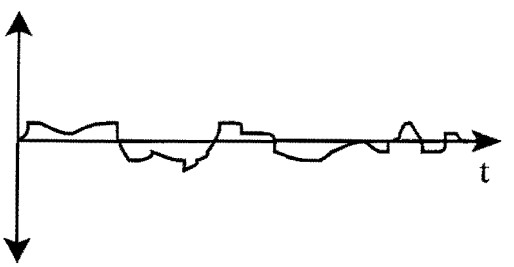

Figure 11: Time history of random data x(t).

Stationary and non-stationary processes of flow measurement occur in the temporal time sense and also in the spatial sense. For example, consider the random turbulence phenomenon at the locations of three transducers, T1, T2, and T3, spatially separated along a pipe, as shown in Figure 12. If the flow in the system is fully developed then the statistical properties of the turbulence at the three points will be the same and be equivalent to a stationary process. However, if the flow is not fully developed, for instance downstream of a bend in the pipe, the statistical properties of the turbulence at the three points will differ and hence the data from these points would correspond to a non-stationary process (although the data at each point constitute a stationary random process) [35].

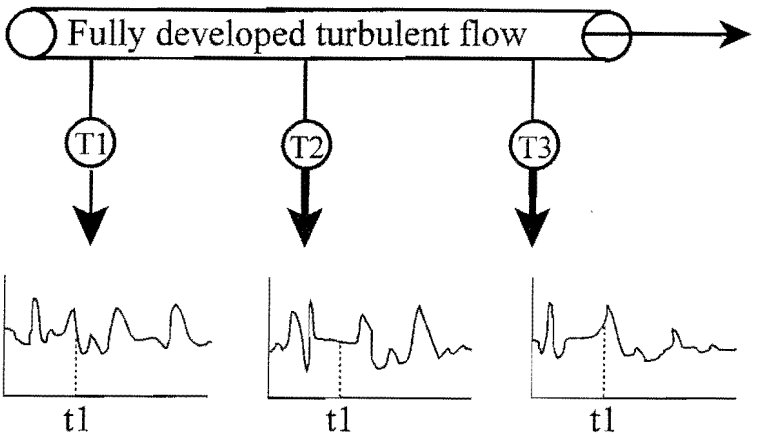

Figure 12: These are the signals obtained from identical transducers in fully developed turbulent flow.

If the process is stationary, the parameters will be time independent and with the parameters estimated by observing the process over a known period of time, the precision of the estimate could be increased by lengthening the observation period. A steady and full developed turbulent flow is an example of an ergodic random process, and the statistical properties of the signal from any one of the tranducers T_1, T_2, and T_3, are always equal to the statistical properties of the set of signals from all the transducers T_1, T_2, and T_3, at any instant in time t_1 $(n\to\infty)$ [35].

The *mean value*, or first moment, μ of a random process is computed as the average of the instantaneous values of a random function of the process, as follows:

$$\mu_x = \lim_{T\to\infty} \frac{1}{T} \int_0^T x(t)dt$$

where μ_x is the mean value of $x(t)$ and $x(t)$ is the instantaneous value, and T the time approaching ∞.

The *autocorrelation function* $R_{xx}(\tau)$ is the joint moment between the values of the random processes at two different times. It can also be calculated as the time average of the product of the instantaneous values *x(t)*, and *x(t+τ)*, over a time *T* approaching infinity, according to the following equation:

$$R_{xx}(\tau) = \lim_{T\to\infty} \frac{1}{T} \int_0^T x(t)x(t+\tau)dt$$

The *mean square value* Ψ_x^2 is equal to the average of the squared value of the time history record *x(t)*, and is given by:

$$\Psi_x^2 = \overline{x^2} = \lim_{T\to\infty} \frac{1}{T} \int_0^T x^2(t)dt$$

In practice, only ac signals are correlated, resulting in an measure of the ac values of the signals, thereby eliminating the effect of the mean value. These parameters are described by the variance and standard deviation of the signal [35].

The *variance* σ_x is defined as the mean square value about the mean μ_x and is given by the equation:

$$\sigma_x^2 = \lim_{T\to\infty} \frac{1}{T} \int_0^T (x(t) - \mu_x)^2 dt$$

The variance describes the dynamic component of the physical data, and the *standard deviation (standard error)* SD is the positive square root of the variance given by the formula:

$$SD = {}^{+}(\sigma_x^2)^{\frac{1}{2}}$$

3.3 Properties of the Autocorrelation Function

The autocorrelation function of random data describes the general dependence of the values of the data at one time t on the values at another time $(t+\tau)$, as shown in Figure 13. This value is obtained by averaging the instantaneous product of the two values $x(t)$ and $x(t+\tau)$ over a time T approaching infinity.

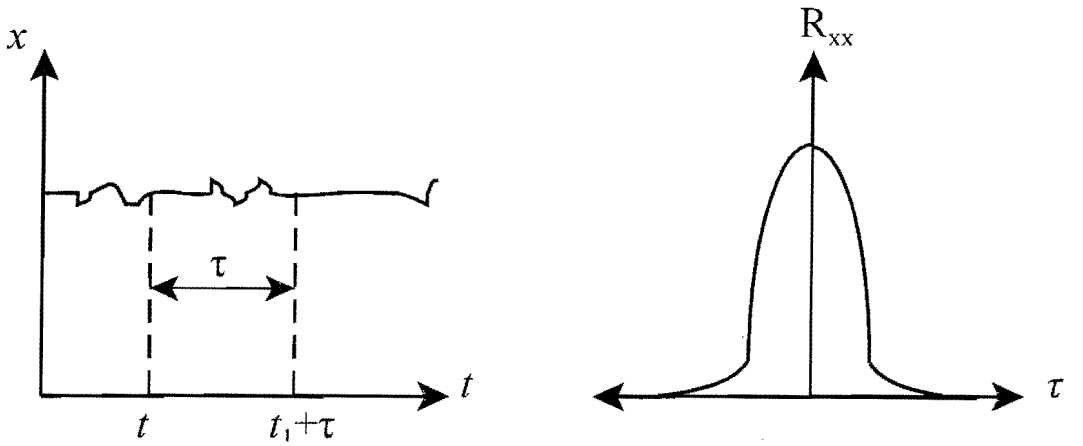

Figure 13: The autocorrelation function of random data describes the general dependence of the values of the data at one time τ on the values at another time $(t+\tau)$.

The autocorrelation $R_{xx}(\tau)$ is a real-valued even function of τ with a maximum at $\tau = 0$; [24] thus

$$R_{xx}(\tau) = R_{xx}(-\tau)$$

and

$$R_{xx}(0) \geq |R_{xx}(\tau)| \quad \text{for all } \tau$$

If the data to be correlated does not include a periodic component, then the mean value μ_x and the autocorrelation function are related as shown in Figure 14, by:

$$\mu_x = \left(R_{xx}(\infty)\right)^{\frac{1}{2}}$$

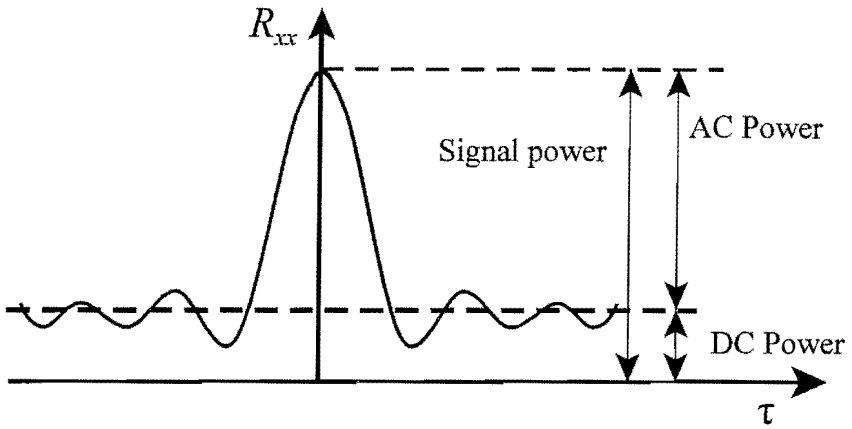

Figure 14: Autocorrelation function of an non-deterministic process, except for a DC component.

If the correlated data *x(t)* has a periodic component, then the autocorrelation function $R_{xx}(\tau)$ will also have a periodic component with the same period, but the phase angle information will be lost [25].

The power of the signal *x(t)* can be defined as its mean square value:

$$Power = E\left(x^2\right) = \overline{x^2}$$

where E indicates the expected or average value. The signal is made up of AC and DC components being; $x_{DC} + x_{AC}$. From this it follows that the power is given by:

$$E(x^2) = E(x_{DC} + x_{AC})^2$$
$$= (x_{DC})^2 + 2(x_{DC})E(x_{AC}) + E(x_{AC})^2$$

With the expectation value $E(x^2_{AC})$ being equal to the variance and assuming that E is a linear operator, the DC signal is constant, and the AC signal has zero mean, we can ignore the middle term and the mean square value now becomes:

$$\overline{x^2} = \mu_x^2 + \sigma_x^2$$

In an ergodic process (such as the turbulent signal from an transducer measuring steady-state flow), which is entirely non-deterministic except for a possible DC component, the value of its autocorrelation function at a time delay of $\tau \to \pm\infty$, is equal to the square of its DC value. Hence

M S Beck and A Plaskowski [35] said, all memory (deterministic relationship) except for that contained in the DC signal, between a pair of observations at a time delay τ apart, vanishes as $\tau \to \pm\infty$. In cross correlation flow measurement systems the existence of a periodic component suggests that there is a pulsation in the flow, or some periodic interference in the transducer output signal.

3.4 Boundary Layer Concept

Whenever a fluid flows over a solid surface, a fluid layer of a definite thickness forms immediately adjacent to the surface. Within this layer the velocity of the fluid undergoes considerable change. This fluid layer is known as the boundary layer, and forms the resistance to heat transfer between the fluid and the solid surface. The concept of the boundary layer is shown in Figure 15.

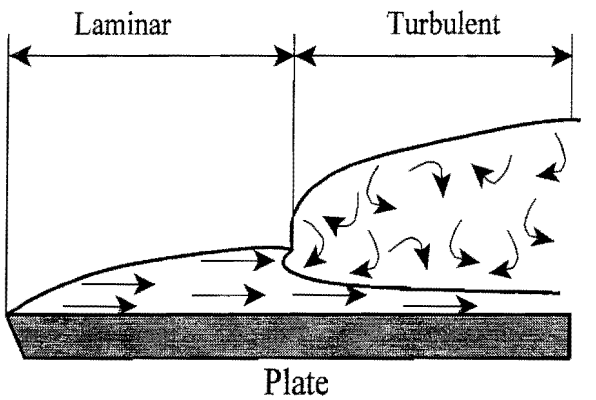

Figure 15: The figure shows the flow being laminar near the leading edge, and becoming more turbulent with air molecules mixing with the flow. Within this turbulent layer the flow may be considered in three layers, namely the laminar sub-layer, buffer layer, and the turbulent layer.

Near the leading edge of the electrode the flow in the boundary layer is characterised by being laminar, allowing very little mixing of the air molecules at different vertical distances above the electrode. At some distance from the leading edge the flow becomes more complex with air molecules mixing with each other. Within this turbulent boundary layer the flow may be considered in three layers namely, the laminar sub-layer, buffer layer, and the turbulent layer.

3.4.1 Air Flow

When air flows from left to right at a velocity U_∞ over a flat solid plate, a boundary layer begins to form. The thickness of the layer, δ is zero at the leading edge and increases with distance x from the leading edge.

The layer of air in contact with the electrode is at rest and hence has zero velocity. At a vertical distance δ from the electrode, the velocity of the air is varies from zero to U_∞. At any distance greater than δ from the electrode the velocity is constant. This change in the velocity of the air in the boundary layer with vertical distance is shown in Figure 16.

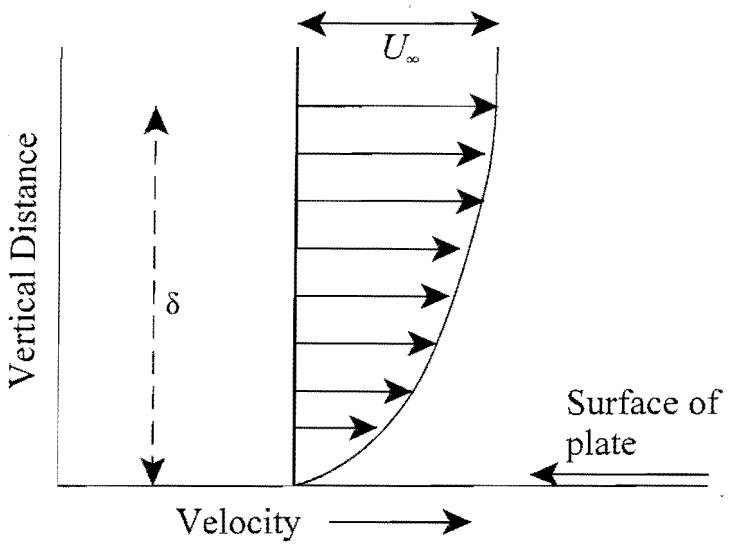

Figure 16: The change of air velocity varies with the change in vertical distance.

3.5 Characteristics of Pipe Flow

The viscosity in fluids greatly affects the flow of the fluid. Viscosity introduces resistance to motion by causing shear or friction forces between fluid particles and the boundary walls of the pipe in which the fluid is present. The effects of viscosity cause the flow of real fluid to occur under two very different regimes: that of laminar flow and that of turbulent flow [25]. This characteristic is defined by a dimensionless term called the Reynolds number:

$$\mathrm{Re} = \frac{\bar{u} D \rho}{\mu}$$

where $\bar{\mu}$ is the mean velocity of the flow, D is the diameter of the pipe and ρ and μ are the density and dynamic viscosity of the fluid. Laminar flow occurs for Reynolds numbers below about 3000; above this value the flow will be turbulent.

3.6 Sensing Techniques

Sensing devices for cross correlation flowmeters can be subdivided into four groups namely;

- Modulation of external radiation by some property of the flowing fluid.
- Emission of radiation by the flowing fluid.
- Instantaneous measurement of changes in capacitance, thermal or electrical conductivity.
- Tagging markers injected into the flowing fluid.

3.7 Modulation of External Radiation

The measurement method involves the projection of a beam of radiation (ultrasonic, gamma rays, or light) across the flow stream, and modulating this beam with the turbulent property of the fluid. If two such beams are spaced axially along the flow, the cross correlation between the received beams is a measure of the flow velocity. The following advantages of external radiation methods exist in certain applications [35]:

- The beam averages the flow information within its cross section.
- The sensors in some applications can be non-intrusive and mounted on the outside of the pipe.
- Transducers can monitor the flow of single-component clean liquids by measuring the natural turbulence in the liquid.
- The performance is essentially independent of temperature, pressure, and viscosity of the fluid.

The following disadvantages must also be considered:

- The detection by means of radiation may increase the cost.
- Accurate positioning of the sensors is important to avoid a mismatch of upstream and downstream signals resulting in incorrect readings.
- A non-linear response to the concentration of the conveying component in the fluid may affect the accuracy of averaging the flow profile.
- High temperatures could damage the radiation generators and receivers.

3.8 Ultrasonic Methods

Two different categories exist, namely continuous and pulsed ultrasound. Continuous-wave systems provide high sensitivity and can detect even the basic turbulence of the fluid. The basic electronics is simple, although care must be taken to avoid errors due to phase shifts occurring when continuous ultrasound is used in an acoustically reflective situation such as a pipe. Pulsed ultrasound systems reduce the standing wave problem, but are less sensitive to flow related

turbulence. Standing waves are always generated in the flow pipe due to the reflective nature of the pipe walls. These reflections affect the stability of the standing wave pattern and ultimately affect the accuracy of the system. As the oscillator frequency varies, the acoustic path length between the transmitter and receiver varies, altering the amplitude and phase of the standing wave. The amplitude variations are not very significant, but the variations in phase can cause severe distortions to the cross correlation function. Instability is also due to variations in temperature, flow velocity, and the rheology of the flowing medium. To overcome these problems a closed-loop system using a phase-locked technique can be used to maintain the acoustic path length between the transmitter and receiver. A novel feature described by Nuijtten *et al* [36] is the use of six ultrasonic beams equally spaced along the pipe axis. This enables five cross correlations to be measured and averaged together, increasing the accuracy. An additional feature in this system is the use of simultaneous phase, frequency and amplitude demodulation of the received ultrasound, so that the demodulated signals can be selected or added to give the optimum sensitivity to the conveyed tracer.

3.9 Optical Methods

These methods rely on the absorption, scattering or reflection of incident light from an external light source. Optical methods have a very limited application in industry due to the problems of optical surfaces in industrial environments. For open-channel flow measurement, optical devices are attractive because problems with soiling are not so critical and the optical systems can provide an accurate, non-contacting method of velocity measurement. A significant problem with light-absorption methods is that the incident radiation is focussed directly onto the photodiode, reducing the modulation capabilities due to the high standing light level. A problem with the low modulation index of the received light is that the random noise generated by the photo-detector decreases the signal-to-noise ratio, reduces the cross correlation coefficient and increases the error. Light-scattering methods prevent the light source from falling onto the photo-detector thereby reducing the saturation effect of the photo-detector. The measured signal is functionally related to the particles in the flow regime. Reflection methods are used in pipe flow and sometimes in moving-bed flow where the particle loading is high. Absorption or scattering methods are not suitable in these applications due to poor light penetration. The use of filament

lamp light sources complicates the scattering process because the photo-detector not only detects the light at a desired angle from the source, but also detects other scattered light of the flow at other angles [37].

With the use of laser light the total optical system can be more closely defined by reducing the range of wavelengths produced. The twin-spot laser cross correlation system measures the transit time of particles between accurately spaced laser beams by cross correlating the outputs of two photo-multiplier tubes focussed onto the measurement zone. The laser beam can come from two separate lasers or from a single laser source with a beam splitter [37]. Figure 17 shows the method of twin-spot laser cross correlation.

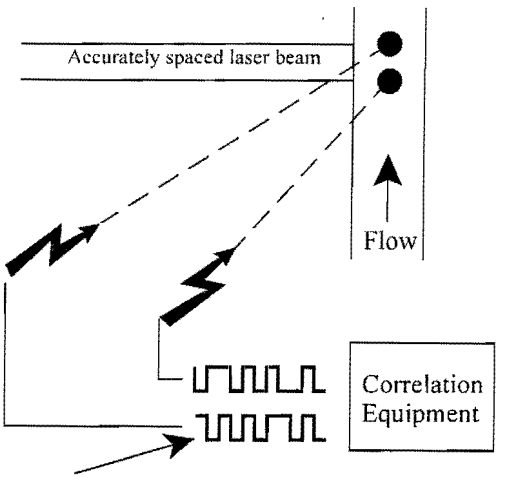

Figure 17: The twin-spot laser cross correlation system measures the transit time of particles between accurately spaced laser beams by cross correlating the outputs of two photo-multiplier tubes focussed onto the measurement zone [37].

One of the most powerful research tools in flow measurement is the laser velocity meter, which relies on the fringe pattern generated by the intersection of two beams of monochromatic radiation from the same laser. Fringes occur at the intersection of two beams, and when particles in the flow pass through the fringe pattern they generate a scattered light signal with a frequency proportional to the velocity of the particles. The scattered light is detected by a photo-detector and the frequency is measured, either by a frequency meter or by using a cross correlator and the generating the Fourier transform of the cross correlation function. An advantage of using the cross correlation method of frequency measurement is that each photon event can be counted.

3.10 Gamma Ray Methods

Gamma photons only react with matter on rare occasions and if interactions do occur the photon vanishes instantly, or at least loses the major part of its energy. The probability that any gamma photon will be absorbed in passing through the thickness of that particular material is a function only of the original energy of that photon, and independent of the thickness of the material through which the photon has already passed [38]. Referring to Figure 18, the absorption for a narrow collimated beam of gamma photons is described by the exponential law to be;

$$I = I_o \exp(-Ex)$$

where I_o is the original intensity, I the final intensity, x the absorber thickness in centimetre, and E is the microscopic cross section of all nuclei in 1 cm^3 of the target material.

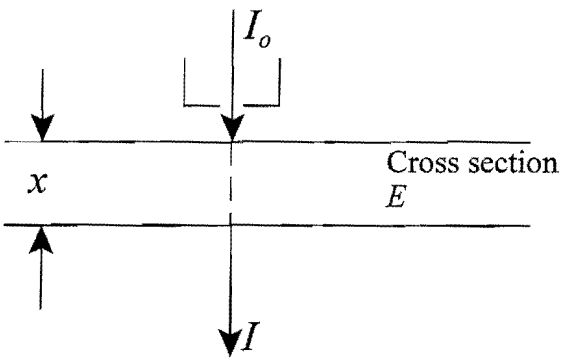

Figure 18: The absorption method of gamma radiation is calculated where: I_o is the original intensity, I the final intensity, x the absorber thickness in centimetre, and E the microscopic cross section of all nuclei in 1 cm^3 of the target material [38].

The microscopic cross section can be redefined in terms of the mass absorption coefficient to be;

$$E_m = \frac{E}{\rho} cm^2 g^{-1}$$

where ρ is the density of the absorber material. By substituting, the final intensity equation shows that the received radiation depends directly upon the thickness x and the average density ρ;

$$I = I_o \exp(-E_m \rho x)$$

3.11 Capacitance Cross Correlation

Capacitance methods of cross correlation flow measurement are based on the measurement of the transit time of the change in the dielectric properties of the flow as it passes sensors located on the axis of a pipe, as shown in Figure 19.

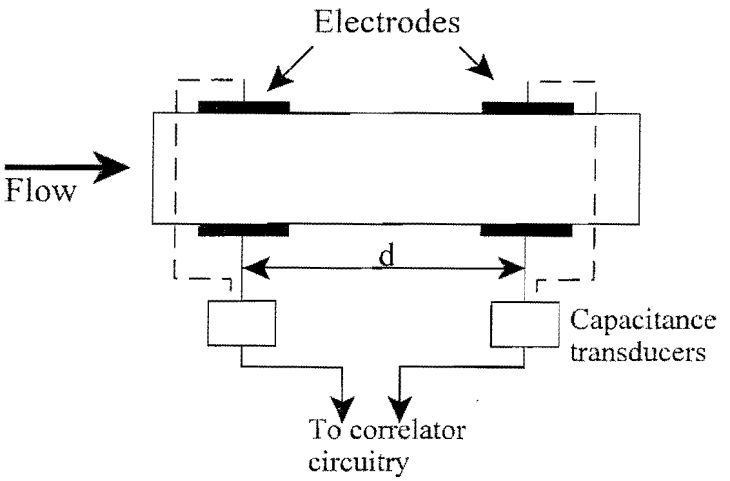

Figure 19: Capacitance methods of cross correlation flow measurement is based on the measurement of the transit time of the change in the dielectric properties of the flow as it passes sensors located on the axis of a pipe.

In the case of a non-conducting liquid or a gas flow, the presence of any dielectric discontinuity (solid, liquid or gas) causes 'dielectric noise', which can be detected and cross correlated by means of capacitance sensors [37]. Capacitance techniques can also be used with conducting fluids provided the excitation frequency is sufficiently high and that the electrodes are insulated from the flow medium to prevent short-circuiting the system [39]. The flow velocity can be determined by cross correlating the dielectric disturbances in the flow that would cause variations in the measured capacitance. It is apparent that if there are any charging effects in the fluid (not necessarily generated by the capacitance measurement system), these will influence the capacitance measuring system readings. Fortunately in many cases both the dielectric changes and the electrostatic charge in the fluid are conveyed at the same velocity, and hence it is not essential to distinguish the charge effect from the dielectric effect when using a cross correlation flowmeter [37]. Electrostatic charging effects are present in the pneumatic conveying of solid materials, and in such cases M S Beck and A Plaskowski [35], found it possible to use this electrostatic charge signal for cross correlation flow measurement. Electrodes for the electrostatic measurement are simpler because such measurements are unaffected by vibration, whereas

capacitance measurements will be strongly affected by vibration if relative movement takes place. However, one general advantage of capacitance sensors is that by using suitable electrode design and guard ring techniques it is possible to obtain uniform field sensitivity over the whole of the pipe cross section, whereas electrostatic sensors are always primarily sensitive to charged material in their vicinity [40].

A wide range of static capacitance transducers have been used for flow measurement with particular interest in the charge transfer system, in which the source electrode is driven by an AC generator and the detector source electrode is connected to a circuit which measures the current and phase shifts relative to the AC generator [22]. The current is a direct function of the impedance between the electrodes, and the phase shift can be used to provide additional information about the loss angle of the dielectric medium. For flow measurement only the current is used as a measured signal. A basic charge transfer transducer including the grounded potential guard ring is shown in Figure 20.

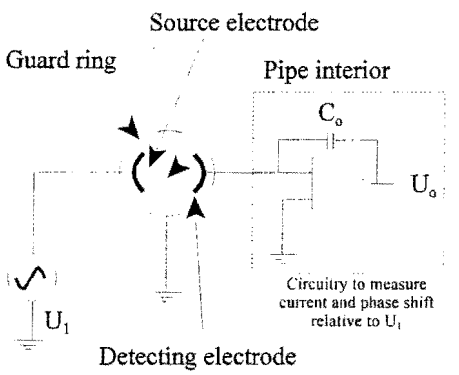

Figure 20: A typical charge transfer transducer consists of a AC signal generator U_1 , source electrode, detecting electrode, and circuitry to measure the current and phase shift of the output U_0, relative to the signal generator, U_1. The earthed guard ring is also shown.

Chapter 4:

ARTIFICIAL NEURAL NETWORKS

4.1 Neural Networks: Background

Many tasks which seem natural for us, such as reading a handwritten note or recognizing a face, are demanding for even the most advanced computer. In an effort to increase the computer's ability to perform such tasks, programmers began designing software to act more like the human brain, with its neurons and synaptic connections [41]. The field of artificial neural networks is used to substitute the traditional method of one central processor to carry out many instructions one at a time, by neural network software which analyses data by passing it through several simulated processors which are interconnected with synaptic-like "weights". Although the programming and mathematics behind neural network technologies are complex, the use of neural network software such as the Matlab Neural Network Toolbox simplifies this process. Once one has collected several records of the data one wishes to analyse, the network will run through them and "learn" how the inputs of each record may be related to the result [41].

Each record in our current work is a set of 28 measurements obtained from the capacitance electrodes and related hardware. All the record's inputs such as the different measurement potentials between the capacitive electrodes, and its related output, (such as: was the dielectric constant of the material detected within the range?) are fed into the neurons of the network. The network then continually refines itself until it can produce an accurate response when given those particular inputs.

After training on several sets of 28 data measurements, the network begins to organize itself, and refines its own architecture to fit the data, much like a human brain "learns" from example. If there is any overall pattern to the data, or some consistent relationship between the inputs and result of each record, the network should be able to eventually create an internal mapping of weights that can accurately reproduce the expected output.

4.2 Basics of Neural Networks

As mentioned earlier, Artificial Neural Networks (ANNs) are able to solve difficult problems in a way that resembles human intelligence. Neural networks have the ability to learn by example, whereas traditional artificial intelligence (AI) solutions rely on the symbolic processing of the data, which requires *a priori* human knowledge about the problem. Also, neural networks techniques have an advantage over statistical methods of data classification because they are distribution-free and require no *a priori* knowledge about the statistical distributions of the classes in the data sources in order to classify them [42].

The model neuron shown in Figure 21 has N input lines and a single output. Each input of a model ANN is weighted or multiplied by the weight value of the corresponding input line. The neuron will provide an output by summing the weighted inputs with reference to a threshold value and an activation function.

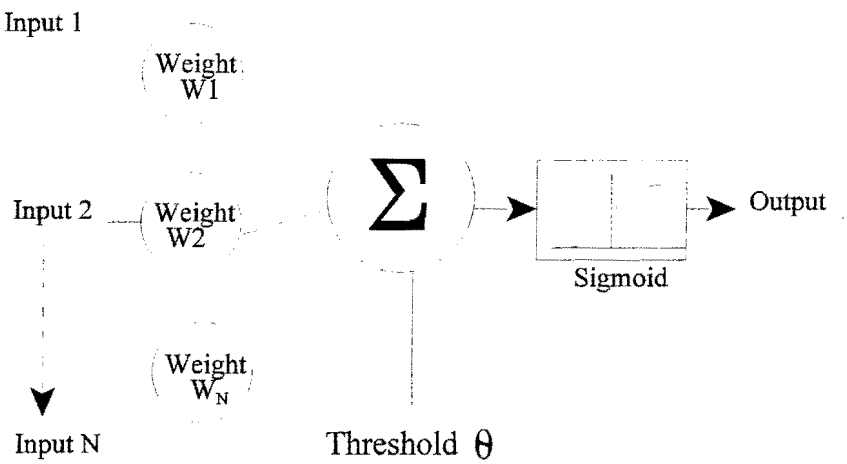

Figure 21: Diagram of a model neuron, showing the inputs applied to different weights, and summed to a threshold value. The activation sigmoid function is differentiable, which is an important feature of ANNs [42].

The neuron has been expressed in mathematical terms below:

$$u = \sum_{i=1}^{N} W_i X_i$$

and

$$y = f(u - \theta)$$

where:

$X_1, X_2, \ldots X_N$ are the input signals.

$W_1, W_2, \ldots W_N$ are the synaptic weights.

u is the activation potential of the neuron.

θ is the threshold.

y is the output signal from the neuron.

$f(u,\theta)$ is the activation function.

The activation function defines the output of the neuron in terms of the activity level at its input. The most common form of activation function used in the construction of ANN's is the sigmoid function. The sigmoid or logistic function is defined by:

$$f(u) = \frac{1}{1 + \exp(-au)}$$

where a is the slope parameter of the sigmoid function. This parameter can be varied to obtain sigmoid functions of different slopes. In the limit, as the slope parameter approaches infinity, the sigmoid function becomes a threshold function [42]. The threshold function can only take the values 0 or 1, whereas the sigmoid function assumes a continuous range from 0 - 1. The sigmoid function is also differentiable which is a important feature in the learning process of ANNs.

4.3 Neural Networks Learning Paradigms

The ability of networks to learn from their environment, and to improve their performance through learning is one of the main advantages. ANNs learn about their environment through an repetitive process of adjustments applied to their free parameters which are the synaptic weights and thresholds. The type of learning is determined by the manner in which the parameter changes take place. There are three basic types of learning paradigms: supervised learning, reinforcement learning, and self-organized (unsupervised) learning.

Supervised learning is performed under the supervision of an external "teacher", providing the network with a desired response for any input vector. The response of the network to each input vector is then compared with the desired response needed for that vector, and the network parameters are adjusted to minimize the difference between the desired response and the actual response. At this stage the network is believed to have built internal representations of the data set by detecting its basic features, and hence, to be able to deal with data that has not encountered during the learning process, that is, it can generalize its "knowledge". Supervised learning is by far the most widely used learning technique in ANNs because of the development of the back-propagation algorithm. Back-propagation is a popular method because it is a computationally efficient method. It also has many limitations that prevent it from always providing solutions for all solvable problems [42].

4.4 Supervised Learning (Back-Propagation Algorithm)

The most frequently used and effective supervised learning algorithm used in ANNs is the development of the back-propagation algorithm in 1986 by Rumelhart, Hinton and Williams [43]. The subsequent publication of the book "*Parallel Distributed Processing: Explorations in the Microstructures of Cognition*" by Rumelhart and McClelland proved that there are can indeed exist algorithms for the training of multilayer perceptrons [44].

Although there are many different kinds of learning rules used by neural networks, this explanation concerns only the *Delta rule*. The delta rule is often utilized by the most common class of ANNs called 'back-propagational neural networks' (BPNNs). Back-propagation is an abbreviation for the backwards propagation of error.

With the delta rule, as with other types of back-propagation, 'learning' is a supervised process that occurs with each cycle or 'epoch' (i.e. each time the network is presented with a new input pattern) through a forward activation flow of outputs, and the backwards error propagation of weight adjustments. More simply, when a neural network is initially presented with a pattern it makes a random 'guess' as to what it might be. It then sees how far its answer was from the actual one and makes an appropriate adjustment to its connection weights [41].

The basic idea of the way this algorithm works is the following:

First an input pair from the training data set is chosen randomly. The input pattern of the pair is given to the network at the input layer by assigning each signal of the pattern to one neuron on this layer. Then, the network passes these signals forward to the neurons on the next layer (hidden layer). For each neuron on the hidden layer, a *Net Input* value is computed, by doing the sum over the products of the output of each neuron on the input layer (which is the original signal itself) by the weight of the connection that connects it to the neuron on the hidden layer in question. When all the neurons on this layer have received a Net Input, the next step for each of these neurons is to compute, from its Net Input, an activation value which is also considered as it's output.

This process is done using a transfer function, usually the *Sigmoid* function as shown in Figure 22.

The output values of the neurons on the output layer are taken as one pattern of signals which is considered as the *actual* output pattern of the network. If the value of this error is zero, there will be no need to make any changes in the connectivity state. However, if the error value is not zero, some changes are to be made in the weights of the connections in the network to reduce this error. During the forward pass the synaptic weights of the network are fixed. During the backward pass, on the other hand, the synaptic weights are all adjusted in accordance with an error signal which is propagated backward through the network against the direction of synaptic connections. This involves sweeping the error backwards through the network and at each layer (level) and changing the weights of the connections [41]. Each weight is either increased by some fraction or decreased. More graphically, the process is shown in Figure 22.

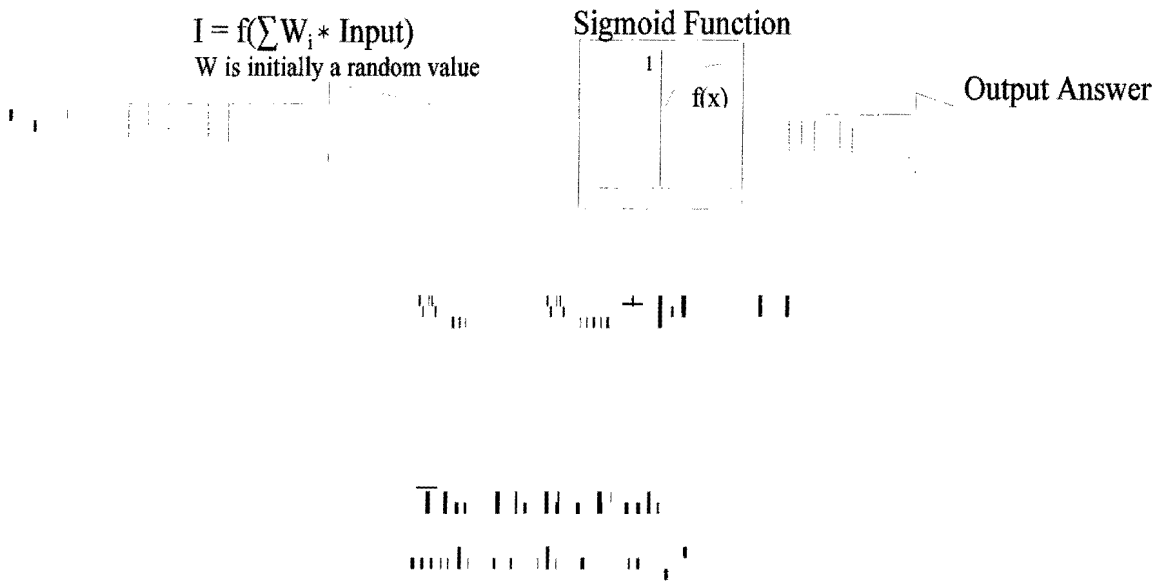

Figure 22: The supervised process occurs with each cycle or epoch, and is performed with feedforward nets where training patterns are composed of two parts, an input vector *I* and an output vector W_{new}, associated with the input and output nodes respectively. The training cycle starts when a forward pass is done and the errors or discrepancies, between the desired and actual response for each node in the output layer are found. The backwards error propagation of weight adjustment according to the magnitude of error ($W_{old}+\beta E_x$) is passed to the input and tested by the network again.

The mathematical formula used by this algorithm is known as the *Delta Rule.* which is the amount by which the weight should change correspondingly to the training pattern pair. The learning rate is a value that must be chosen between 0 and 0.9. It determines the size of the step by which the neural network system moves towards an optimal state. The actual idea behind the back-error propagation algorithm is to slide along the error surface performing a gradient descent in search of, ideally, what is known a global minima (a state of the network where the error on its output patterns is optimal (minimum). The global minimum is that theoretical solution with the lowest possible error.

The diagram below shows an example of what is known as a local minima, which is simply an area on the error surface where the error of the system drops down [44].

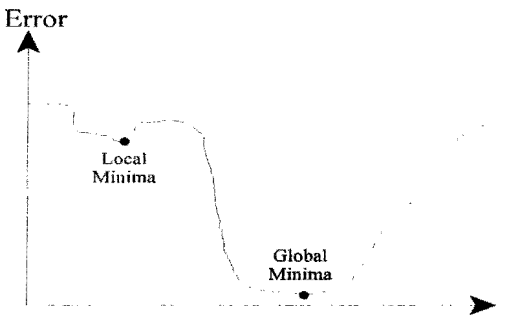

Figure 23: Example of local and global minima.

Choosing a value for the learning rate is very delicate, because, if it is assigned a large value, then local minimas can easily be avoided by just jumping over them. The result could be system oscillations, jumping forward and backward over the global minima without ever getting there. However, if the learning rate is set to a small value, then the global minimas cannot be missed, but the system is more likely to be trapped in a local minima. For this reason a new variable has been introduced, known as the *Momentum (β)*, whose value should be in the range 0 to 0.9 as well.

Most learning rules have built-in mathematical terms to assist in this process which control the 'speed' β, and the 'momentum' of the learning. The speed of learning is actually the rate of convergence between the current solution and the global minimum. Momentum helps the network to overcome obstacles (local minima) in the error surface and settle down at or near the

global minimum. In this way, the learning rate value can take a large value and the risk of ending up in an oscillating state is minimised.

This whole process is done for each and every example set and for many epochs. Once a neural network has been trained to do a certain task, it should then be validated. The process of validation is in other words a process of checking its performance. This is done by providing a set of pairs of input/output patterns which is similar to the training set used to teach the network but different in contents. With this set of data, the input patterns to the network are given, and the output produced is observed. It is then compared to the target output. A judgement on the overall performance of the network, including whether some more training is required or not, is taken at this point. Once the network is fully trained and validated, it can then be used as a black box system.

Since the nature of the error space can not be known *a priori*, neural network analysis often requires a large number of individual runs to determine the best solution.

It is also possible to over-train a neural network, which means that the network has been trained exactly to respond to only one type of input. In real-world applications this situation is not very useful since one would need a separate network for each new kind of input.

4.5 Summary

The advantage of ANNs are their flexibility against distortions in the input data and their capability of learning. They are often good at solving problems that are too complex for conventional technologies (e.g., problems that do not have an algorithmic solution or for which an algorithmic solution is too complex to be found). In our case the application of ANNs is the capturing of certain associations between materials or discovering regularities within a set of patterns in capacitive tomography applications. It would also be useful to determine the volume, number of variables, diversity and relationships between variables which are vaguely understood.

Chapter 5:

TOMOGRAPHY SYSTEM DESIGN

This chapter is an overview of the methods used in the design and construction of the static tomography vessel used in the experiments discussed in Chapter 6. Sections covered include:

- The design layout of the capacitive sensing electrodes.
- The unique capacitive electrode numbering system used, as well as the various electrode combinations.
- The interfacing of the tomography system to the computer.
- The mathematical calculations of the sensing areas, and how this relates to the measurements obtained.
- The tomographic hardware and software implementation of the system.

5.1 Design and Construction of the Static Vessel

The capacitance electrodes can be mounted either inside or outside the vessel. If the vessel wall is an electrical insulator such as plastic, then the electrodes are normally mounted on the outside surface of the pipe or vessel. In our case, the measurement is non-invasive and can be made intrinsically safe. The sensor is surrounded by an earthed shield which minimizes the influence of external fields or objects. The number and size of the capacitance electrodes used depends on the application. A larger number of electrodes will give a higher resolution image but the measurement sensitivity will be low. The sensitivity can be increased by using longer electrodes but this will lower the axial resolution. If high axial resolution is required, a small number of short electrodes can be used together with separately excited axial guard electrodes, which prevent the electric field from spreading excessively at each end of the sensor electrodes.

Our vessel was constructed from polyester pipe with a wall thickness of 15mm. The inner radius measured 11cm and the height 30cm respectively. Eight capacitive electrodes were mounted around the outer circumference of the vessel with an equal distance of 2cm between the electrodes. The approximate capacitance electrode size was calculated from the formula:

$$C = \frac{KA}{d}$$

where: K is the dielectric constant of the medium, A is the area of the electrode, and d the distance between two parallel electrodes in cm.

The sensing electrodes were cut from 1.2 mm galvanised steel sheets, to the size of 8 x 10 cm and mounted on the outside of the vessel as shown in Figure 24. With a diagonal distance between the electrodes measured at 20 cm, and a dielectric constant of 80.37 for water at 20 °C, and 78.54 for water at 25 °C [45], the approximate capacitance between the electrodes, (with water as the dielectric medium) was calculated to be approximately 320 pF. A grounded guard rail was mounted around the outside of the vessel to minimise the influences of external stray capacitances, as shown in Figure 25. The redundant electrodes are always connected to earth forming 'guard rings' and enabling the measurement sensitivity to be focussed between the selected electrode pair.

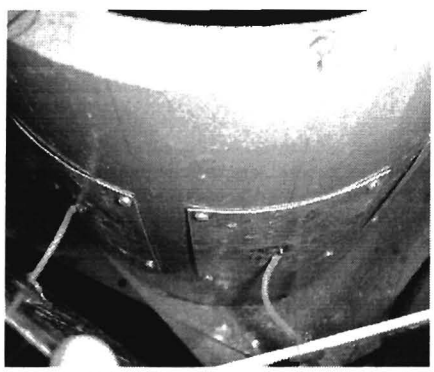

Figure 24: The photograph shows the sensing electrodes mounted externally on the wall of the pipe.

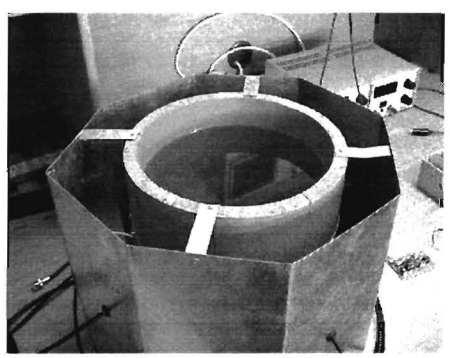

Figure 25: The photograph shows the polyester pipe surrounded by 8 capacitive sensing electrodes including the earthed shield which minimizes the influence of external fields or objects.

5.2 Interfacing the Static Vessel

In order to retrieve information from the vessel, the interfacing of the sensor electrodes to the capacitance/conductance synchronous detection system is performed by the PIC16C73 micro-controller and MAX350 serially controlled multiplexer switches and reed relay contacts, as shown in Figure 26.

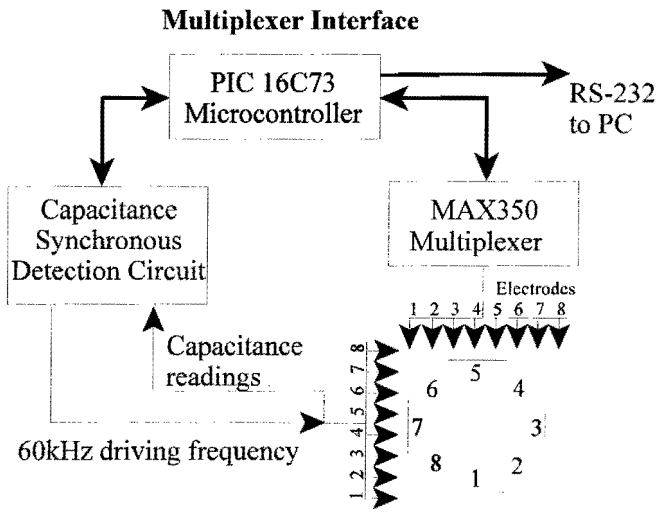

Figure 26: The diagram shows the PIC16C73 controlling the process of selecting the correct capacitance electrode combination, as shown in Table 1, and switching this capacitance measurement through to the capacitance synchronous detection circuit. Once the capacitance/voltage conversion has been done, the PIC16C73 performs the digital conversion of this reading and transmits this to a PC via a RS-232 link.

Initially the use of semiconductor multiplexer switches affected the readings obtained due to the on-resistance and on-capacitance of the contacts. To solve this problem, reed relay contacts were introduced in addition to the semiconductor MAX350 multiplexer switches, which minimised the effects of switch contact resistance and capacitance. Eight-bit analog to digital conversion is performed by an PIC16C73 micro-controller, which also controls the serial data transmission to the PC. Five sets of 28 readings taken in 1 second intervals are logged, resulting in a total of 140 independent measurements. This number can be adjusted to accommodate more readings at different intervals, as required by the application. The electrodes were numbered according to the method shown in Figure 27, and all readings were taken in an anti-clockwise direction, starting with electrode 1 as the master driving electrode.

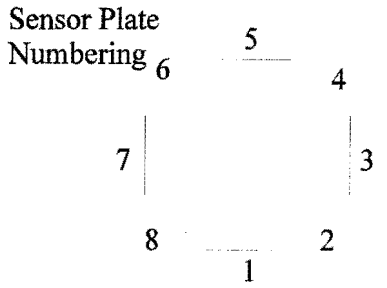

Figure 27: The sensor electrode numbering method indicated, was used to perform the 28 measurement combinations between the driving and sensing electrodes.

In the 8-electrode tomography system we designed, the capacitances between electrodes 1 and 2, then 1 and 3, and so on up to 1 and 8 (with electrode 1 being the driving electrode, and electrodes 2, 3, 4, ..., 8 being the sensing electrodes) are measured and fed to the data collection system. Next, electrode 2 is selected as the active or driving electrode and the capacitances between electrodes 2-3, 2-3, ..., 2-8 are measured. This order of sensing is shown in Table 1, with a total of 28 independent measurements being made. Five groups of the output $V_{out(Cx)}$ (a function of the sensor capacitance), were measured between the 28 different combinations, supplying a total of 140 measurements. These measurements were averaged and the resultant used in all graphical representations.

The next section discusses the approach we followed to graphically illustrate the data by making use of Matlab. The idea was to weight each area in the zone being sensed against the overall area of the vessel, and to relate this to the dielectric being measured within this area.

The table below indicates the 28 capacitive electrode combinations used for all testing.

Measurement Sequence (1 - 28)	Measurement electrode combinations							
	Electrode 1	Electrode 2	Electrode 3	Electrode 4	Electrode 5	Electrode 6	Electrode 7	Electrode 8
1	●	●						
2	●		●					
3	●			●				
4	●				●			
5	●					●		
6	●						●	
7	●							●
8		●	●					
9		●		●				
10		●			●			
11		●				●		
12		●					●	
13		●						●
14			●	●				
15			●		●			
16			●			●		
17			●				●	
18			●					●
19				●	●			
20				●		●		
21				●			●	
22				●				●
23					●	●		
24					●		●	
25					●			●
26						●	●	
27						●		●
28							●	●

Table 1: The table indicates how the master driving electrode (highlighted section) is selected, and combined with the sensing electrode to form the sensing capacitance. An example would be measurement 1 of 28, where the capacitance is measured between electrodes 1 and 2, with electrode 1 the master driving electrode, and electrode 2 the sensing electrode.

5.3 Electrode Measurement Data Transfer

The active electrodes are switched to the self-tuning capacitance sensor by means of digitally controlled switches. Five complete data collection cycles of all 28 independent measurement combinations are made. These measurements are converted to an analog voltage by the capacitance synchronous detection method, and thereafter converted to the equivalent 8-bit digital code. With a 9600 baud, RS-232 connection to a PC, the data is collected and saved as an image

file. These five sets of data arrays comprising 140 measurements in total are now averaged and displayed on a graph with the use of Matlab.

5.4 A Simple Approximate Reconstruction Method for Display Purposes

We approached each reading as being a measure of the dielectric immediately between the electrodes without any capacitance fringing included (although we realise that this is a considerable simplification). Another simplification made is the assumption that the measurement occurs between two parallel electrodes, with the electrodes covering the entire circumference of the pipe, giving us an octagonal cross-sectional area. This gives us four possibilities for the dielectric distribution:

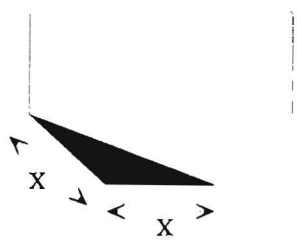

Figure 28: The highlighted section, called a zone in our case, represents the simplified equivalent of the dielectric area between two nearest-neighbour electrodes.

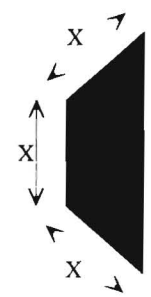

Figure 29: The figure shows the simplified equivalent of the dielectric area or zone between electrodes separated by one electrode length, ignoring any fringing capacitances.

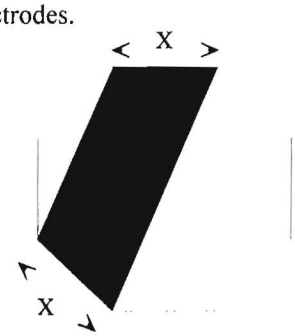

Figure 30: The figure shows the zone area of the dielectric immediately between electrodes separated by two electrode lengths. The fringing capacitance has been ignored.

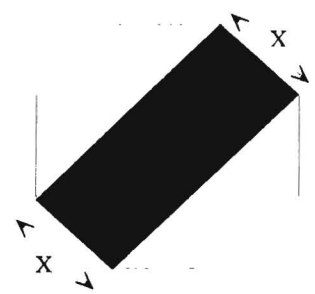

Figure 31: The zone area between electrodes separated by three electrode lengths represent the area of a rectangle when the fringing capacitance is ignored.

From this it can be seen that in each case above the dielectric volume that is sampled will differ in relation to the overall cross-sectional area. The nearest-neighbour electrodes sample a very small volume, whereas electrodes separated by three electrode lengths sample a very large volume.

In order to perform the inverse operation to sampling, the dielectric of a given volume (or area in the cross sectional representation) has to be estimated given the readings obtained relating to the capacitance between the selected electrodes. The starting point to this would be to calculate what each area or zone contributes to a given capacitance reading. If the length of each electrode is X, then the nearest-neighbour electrodes, as shown in Figure 28, sample a zone area of:

$$A_{nn} = X \sin\frac{\pi}{8} \cdot X \cos\frac{\pi}{8}$$

$$= 0.35X^2$$

Electrodes separated by one electrode, as in Figure 29, sample a zone area of:

$$A_{1E} = \frac{X^2}{2} + \frac{X^2}{\sqrt{2}}$$

$$= 1.21X^2$$

Electrodes separated by two electrode lengths, as in Figure 30, sample a zone area of:

$$A_{2E} = 2\left(X \cos\frac{\pi}{8}\right)^2 + 0.35X^2$$

$$= 2.06X^2$$

Electrodes separated by three electrode lengths, as in Figure 31, sample a zone area of:

$$A_{3E} = X^2 + 2X \cdot \frac{X}{\sqrt{2}}$$

$$= 2.414X^2$$

The areas defined in the above calculations subdivide the whole cross section in an overlapping pattern of segments, as shown in Figure 32.

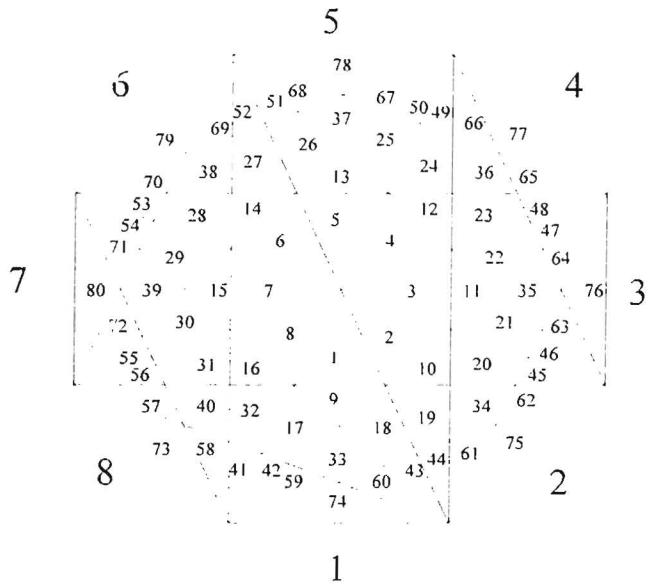

Figure 32: The cross section of the octagonal measurement surface has been numbered in segments, ranging from 1 - 80. Some of the segments have similar areas for example, segments 17, 18, 19, and 32.

Each zone has an certain area related to the dielectric measurement of the capacitance between two electrodes. There are a total of 80 segments in the octagonal cross section, with certain segments excluded when any of the four different zones are selected. For example, when the zone (between electrodes 1 and 4) shown in Figure 33 is selected, the segment highlighted is included in that zone, and has a certain weight when compared to the overall area of that zone.

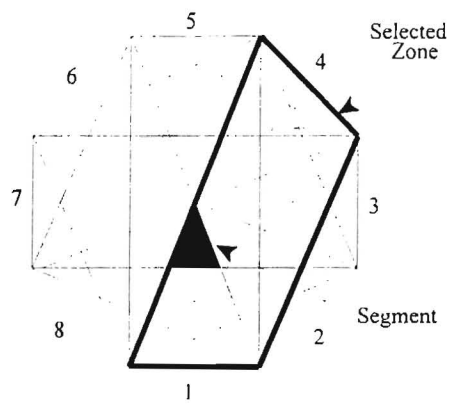

Figure 33: The figure shows the highlighted triangular section, being part of the measurement zone between electrodes 1 and 4.

5.5 Calculation of the Segment Areas

First we need to calculate the area of the triangle, in terms of X:

$$A_{triangle} = \frac{X^2 - \frac{X^2}{\left(1+\sqrt{2}\right)^2}}{8}$$

$$= 0.104X^2$$

We can then define the contribution or weight of any segment to any zone in the cross section, in terms of its area; so that the dielectric of the segment shown in Figure 32, differs according to the overall zone area. This is illustrated in Figure 34.

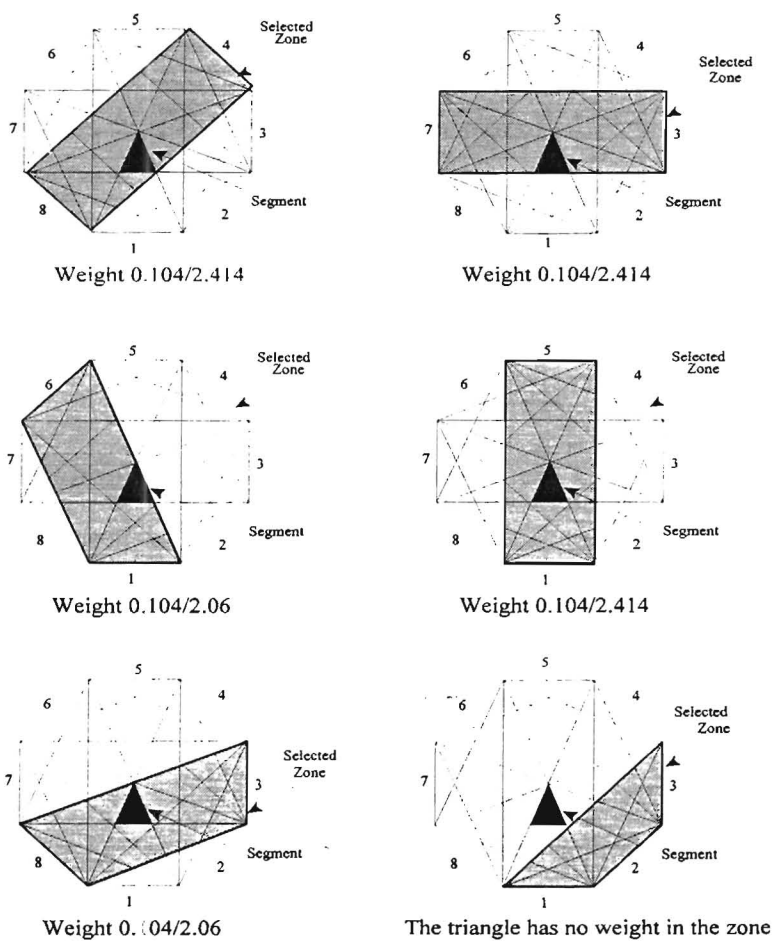

Figure 34: The weights that the highlighted segment contributes to the selected zones are indicated. In the bottom right hand figure it can be seen that the triangle (zone) contributes no weight to the selected zone.

The area of the individual segments shown in Figure 35 were calculated and are summarised below.

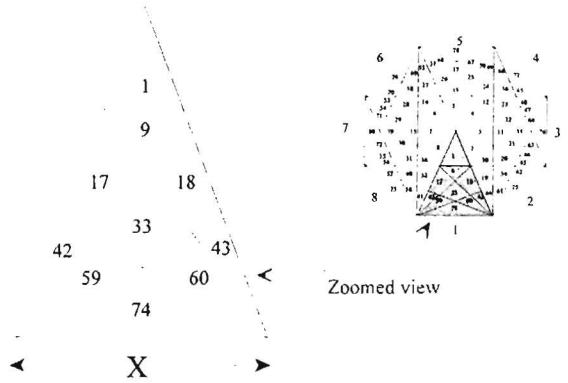

Figure 35: The figure shows a 'zoomed' view of the triangle highlighted on the right. The segments were numbered in an anticlockwise direction around the centre of the octagon. With reference to the larger octagonal version in Figure 31, it can be seen that for example, segments 1 to 8 all have the same area, and segments 9 - 16 have an different area.

Segments	Area
1, 2, 3, 4, 5, 6, 7, 8	0.104 X^2
9, 10, 11, 12, 13, 14, 15, 16	0.0428 X^2
17, 18, 19, 20, 21, 22, 23, 24, 25, 26, 27, 28, 29, 30, 31, 32	0.0731 X^2
33, 34, 35, 36, 37, 38, 39, 40	0.06159 X^2
41, 42, 43, 44, 45, 46, 47, 48, 49, 50, 51, 52, 53, 54, 55, 56	0.0302 X^2
57, 58, 59, 60, 61, 62, 63, 64, 65, 66, 67, 68, 69, 70, 71, 72	0.0427 X^2
73, 74, 75, 76, 77, 78, 79, 80	0.103 X^2

Table 2: The table shows the areas of the segments in relation to the length of the electrode X.

5.6 Area and Dielectric Relationship

The voltage measurements obtained from our synchronous detection capacitance circuitry are equivalent to the capacitance between the selected electrodes. These measurements make up a 28 x 1 vector called C. There are 80 segments in the cross section of the octagonal shape, so we will calculate the dielectric of each zone ε_i using the equation:

$$\bar{\varepsilon} = \bar{\bar{W}}\bar{C}$$

in which W is a 80 x 28 matrix of weights related to the segment area compared to the zone area, as shown in Table 2. A further adjustment that has to be made is the assumption that the measurements are obtained from two electrodes in parallel, where A and d are the area and distance separation of the electrodes respectively.

$$C = \frac{A\varepsilon}{d}$$

While this is not the case in some zone measurements, we will make an assumption of linearity in terms of some constant k for each pair of plates:

$$kC = \varepsilon$$

The constant k could be calculated from first principles, but the answer would be dubious given the high levels of approximation up to this point. It would probably be more accurate to calculate the constant k from a measurement on the uniform dielectric in the actual vessel. The equation would then be:

$$\bar{\varepsilon} = \bar{\bar{W}}\left(\bar{k} \cdot \bar{C}\right)$$

If we have the known values of ε we can solve for k by inverting W:

$$\bar{k} \cdot \bar{C} = \bar{\bar{\varepsilon}}\bar{\bar{W}}^{-1}$$

5.7 Calculating *W*

From the method shown in the previous section, and the results shown in Table 2, it can be seen that *W* can be calculated. Firstly, the order of *C*, which is the column vector of measurements, has to be defined:

Let's assume that *C* is the column vector of 28 measurements taken from our vessel, all with different measured voltages, then:

$C =$

$$\begin{matrix} Z_{1,2} \\ Z_{1,3} \\ Z_{1,4} \\ Z_{1,5} \\ Z_{1,6} \\ Z_{1,7} \\ Z_{1,8} \end{matrix} \quad \begin{matrix} Z_{2,3} \\ Z_{2,4} \\ Z_{2,5} \\ Z_{2,6} \\ Z_{2,7} \\ Z_{2,8} \end{matrix} \quad \begin{matrix} Z_{3,4} \\ Z_{3,5} \\ Z_{3,6} \\ Z_{3,7} \\ Z_{3,8} \end{matrix} \quad \begin{matrix} Z_{4,5} \\ Z_{4,6} \\ Z_{4,7} \\ Z_{4,8} \end{matrix} \quad \begin{matrix} Z_{5,6} \\ Z_{5,7} \\ Z_{5,8} \end{matrix} \quad \begin{matrix} Z_{6,7} \\ Z_{6,8} \end{matrix} \quad Z_{7,8}$$

(Note: this is simply a 28x1 column vector)

5.8 Comparison between our Simple Approximate Reconstruction Method and the Back-projection Image-reconstruction Algorithm

In the mathematical approach used for our simple approximate reconstruction method to produce an image in relation to the measured voltages, the following assumptions were made:

- The conductivity and potential do not change along the length of the cylinder, i.e. the problem is 'two-dimensional'.
- The electrodes are uniformly spaced around the body.
- The cylindrical vessel-wall thickness does not affect the final image.

The first step as discussed in Section 5.5 was to calculate and define the area ratio of any segment to any zone (the area between two electrodes) in the cross section. Next, the mathematical calculations of the dielectr c relationship (*W* matrix) of a zone in the octagonal area, to that of each segment in that zone was completed. An labelled imaginary grid as shown in Figure 37, was placed over the octagonal surface area. By subdividing the entire surface area into 80 different segments, and attaching an equivalent 'dielectric weight' to each segment, we were able to

approximate where the differences in dielectric constants were prominent inside the vessel. In principle our method is invariably a linear operation where a vector of 28 voltage measurements are multiplied by a matrix (W) of weights related to the segment area compared to the zone area.

Back-projection image reconstruction using iterative reconstruction algorithms has proved that the accuracy of the reconstruction improves with each iteration [48]. The LBP method is based on first obtaining the sensitivity distributions, or maps, for all electrode pairs (28 in our case). The normalised capacitance changes between the electrode pairs are then linearly superimposed onto the sensitivity maps to obtain the images. Usually the sensitivity maps are calculated using a finite element (FE) software package.

An initial image is calculated from the set of normalised capacitance measurements and the sensitivity maps, using linear back-projection (LBP). The values of the normalised pixels in this image are then used to back-calculate a second set of capacitance values, using a field solving algorithm. The two sets of capacitances are then compared and the difference between each pair of values is used to generate an error image. The error image is used update the original image, and the field solving algorithm is then used to calculate a new set of capacitances. This process is then repeated several times to obtain a convergent set of images. Approximately 20 iterations are required to obtain good quality images [48].

The weight of the segment shown in the Figure 36, is part of the 'dielectric measurement area' when certain zones have been selected. The first row of matrix W as seen in Table 3, would be:

$$W_{1,n} = (0,\ 0,\ 0.05048,\ 0.0403,\ 0.05048,\ 0,\ 0,\ 0,\ 0,\ 0,\ 0.0403,\ 0.05048,\ 0,\ 0,\ 0,\ 0,\ 0.0403,\ 0.05048,\ 0,\ 0,\ 0,\ 0.0403,\ 0,\ 0,\ 0,\ 0,\ 0,\ 0)$$

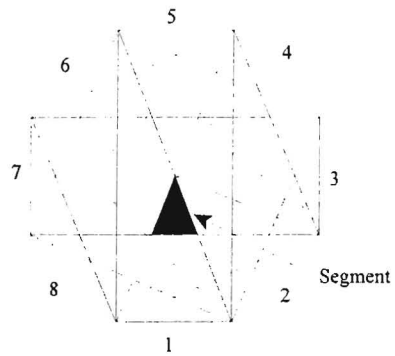

Figure 36: The weight of the segment highlighted would only be used in the calculation of W when the triangle affects the measurement of a zone, and zero otherwise.

Table 3: The highlighted cells in table *W* on the following page is the resultant of the dielectric contribution of each segment in column B, in relation to the selected zone areas (columns C to AD).

5.9 Displaying the Area and Dielectric Relationship in Matlab

After performing the mathematical calculations of the dielectric relationship (W matrix) of a zone (the area between two electrodes) in the octagonal area, to each segment in that zone, the information had to be plotted 3-dimensionally in Matlab. Matlab requires a regular rectangle grid in order to plot 3-dimensional data. We decided to draw an imaginary grid over the octagonal surface area, and to label the grid as indicated in Figure 37.

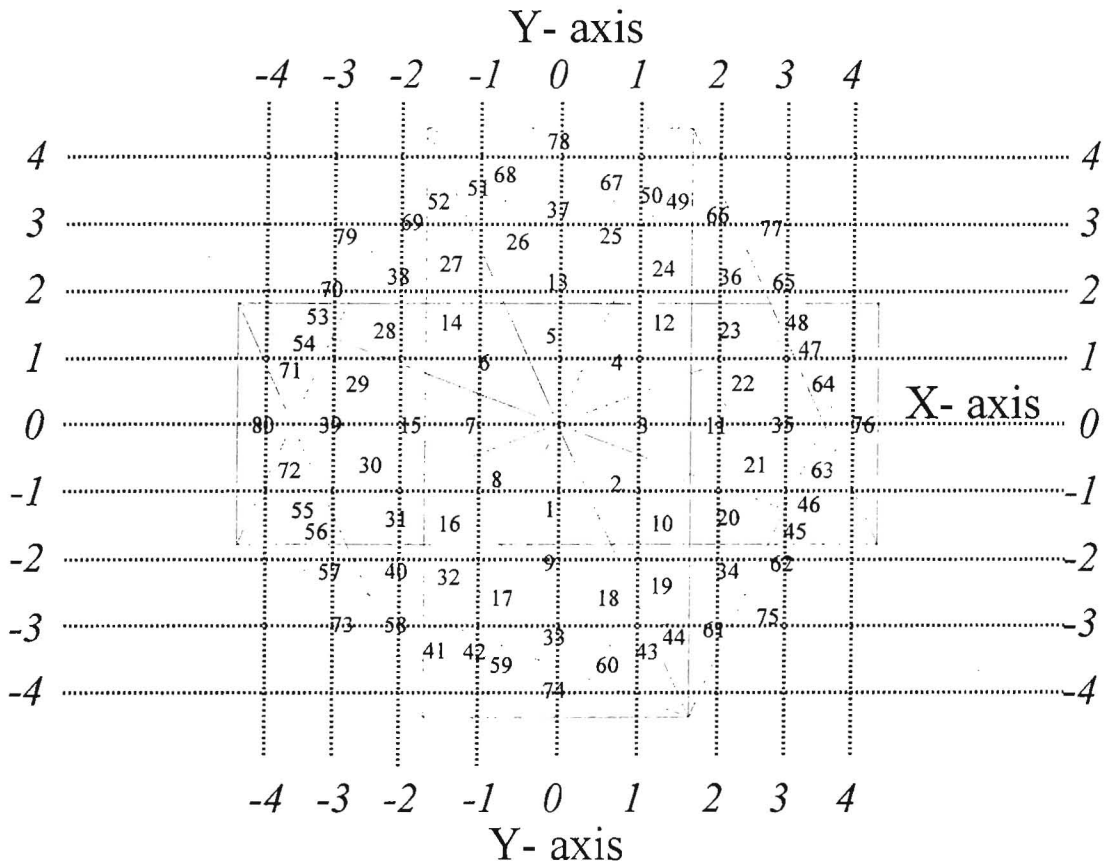

Figure 37: The grid shown on the x-axis and y-axis is used to plot the equivalent dielectric weight contribution of each segment in the W matrix, onto the z-axis of the 3-dimensional surface plot in Matlab.

From this grid the centre position of each segment can be determined, and the dielectric weight of that segment plotted from the calculated values in the W matrix. An example would be when the dielectric weight of the triangle in Figure 36 is plotted, the row in the matrix W would be used:

$W_{1,n}$ = (0, 0, 0.05048, 0.0403, 0.05048, 0, 0, 0, 0, 0, 0.0403, 0.05048, 0, 0, 0, 0, 0.0403, 0.05048, 0, 0, 0, 0.0403, 0, 0, 0, 0, 0, 0)

This dielectric equivalent for the above mentioned segment would plotted on the co-ordinates of the x-y axis at:

-1.4 on the y-axis

and

0 on the x-axis

The Matlab code in Appendix A, shows the programming method followed to plot the 3-D surface plots for all the graphs in the Chapter 6.

5.10 Summary

With the idea of subdividing the entire surface area into 80 different segments, and attaching an equivalent 'dielectric weight' to each segment, we were able to approximate where the differences in dielectric constants were prominent inside the vessel. Our task was not to produce the final image reconstruction of the measured dielectric distribution, but to give some display to the measured values in a 3-dimensional form. The technique we followed was a step towards the implementation of a neural network with the use of back-projection algorithms to produce the image of the dielectric distribution.

Chapter 6:

EXPERIMENTAL RESULTS

This chapter presents the results of static tests performed on the prototype capacitance tomography system using the synchronous detection capacitance measuring method. The primary objective was to assess what the capabilities of the measuring instrument were when discriminating between air, seawater, and rock.

A collection of 16 experiments were performed and are described below, including tests with 100% air, air/sea-water combinations, and air/sea-water/rock combinations.

In order to determine what the capacitive range of the system was, these experiments were completed:

9. To measure the lower threshold of the system with only air acting as the dielectric medium in the vessel.
10. To insert a portion of polystyrene in the centre of the vessel to determine what the resultant output would be when compared to the measurement with only air acting as the dielectric. This would prove to be useful when measurements are made with the polystyrene acting as the air medium.
11. To determine what the upper threshold of the vessel would be with when filled with sea-water only as the dielectric.

All other measurements would fall within this range, thereby pointing out what the range sensitivity of the system would be with various combinations.

The relative dielectric constants shown in Table 4 were used in the calculations and assumptions made in this chapter, and were sourced from the CRC Handbook of Chemistry and Physics, 58th Edition [46].

Dielectric medium	ε 20 °C	ε 25°C
H_2O	80.37	78.54
Air	1.00054 at room temperature	
Polystyrene	2.54 - 2.56 at 25 °C	

Table 4: The dielectric constants used in the calculations are shown in the above table, and were sourced from the CRC Handbook of Chemistry and Physics, 58th Edition [46].

Currently most electrical capacitance tomography systems are calibrated using a lower permittivity material and a higher permittivity, so that the high permittivity material distribution can be imaged on the low permittivity material background. The conventional normalisation approach assumes that the distribution of the materials is in parallel and the normalised capacitance is a linear function of the measured capacitance [49].

$$\lambda = \frac{C_m - C_l}{C_h - C_l}$$

where λ is the normalised capacitance between a pair of electrodes, and C_m is the measured capacitance. C_l and C_h are the capacitances when the system is full of the lower [in our case, air] and higher [in our case, seawater] permittivity materials used to calibrate the system. From the equation shown above the normalised capacitance will be "0" when the vessel is full of air, and "1" when the vessel is filled with seawater.

To normalise our measurements we simply subtracted the voltage readings obtained when the vessel was empty [air only], from those when the vessel was filled with seawater.

In our experiments the normalisation process proved to be difficult with a combination of air and rock samples, as the relationship between the normalised capacitance values and the capacitance readings of the combination [air/rock] are severely non-linear. This is particularly evident when observing the 3-D plots of the rock/air combinations. The vertical axis in the 3-D plots shown in the experiments depict the relative dielectric strength and was calculated by a multiplication of the W matrix, the measured voltages and the relative dielectric constant.

6.1 Experiment 1: 100% Air

The first experiment was performed with 100% air in the vessel to determine what the lower capacitance range of the system would be. From the results in Figure 38, it can be seen that the measurements between the capacitive electrodes produces a flat response over the entire surface area.

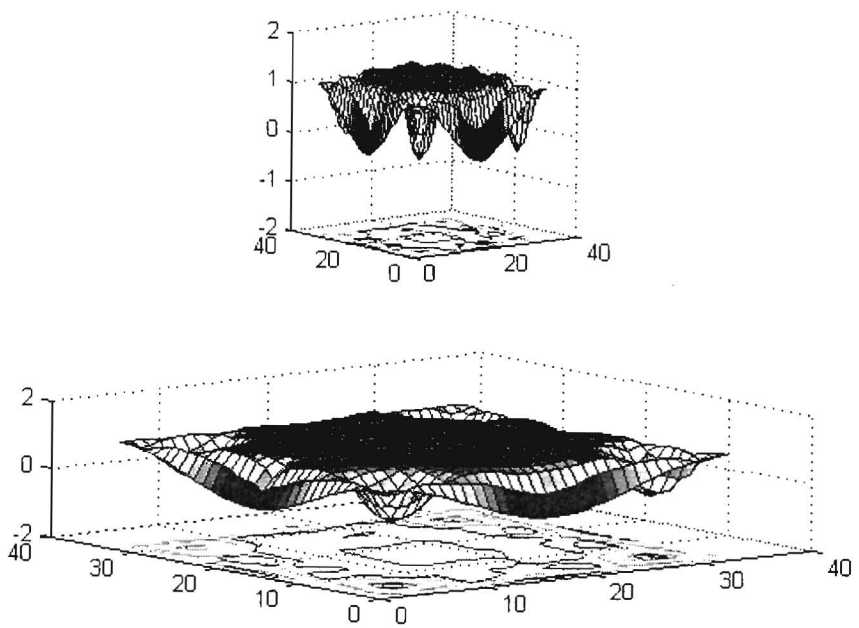

Figure 38: The main plot shows the response of our system when measuring 100% air in the vessel. The cross-section of the pipe can be seen as a darker circle. The subplot shows the same data points been plotted at a different angle to the main plot. The corners of these plots, and all other similar graphs, are outside the pipe, and may be ignored. The horizontal axes are arbitrary co-ordinates.

Most of the reading are concentrated around the dielectric constant of 1.00054 for air. It was noted from the readings obtained, that when electrode 1 as the driving or master electrode, the output voltage varies and decreases to approximately 0.7V when the measurement is made between the furthest electrodes, 1 and 5. This proved to us that the output voltage which is a function of the capacitance, decreases as the distance between the electrodes increases, and increases as the sensing electrode and driving electrodes are closer.

6.2 Experiment 2: Polystyrene and Air in the Centre

With the dielectric constant of 2.54 for polystyrene [45], the following experiment was performed to determine how the system would react when an polystyrene bubble without water, was inserted in the centre of the vessel. Figure 39 shows the size of the polystyrene 'air bubbles' that were inserted into the vessel.

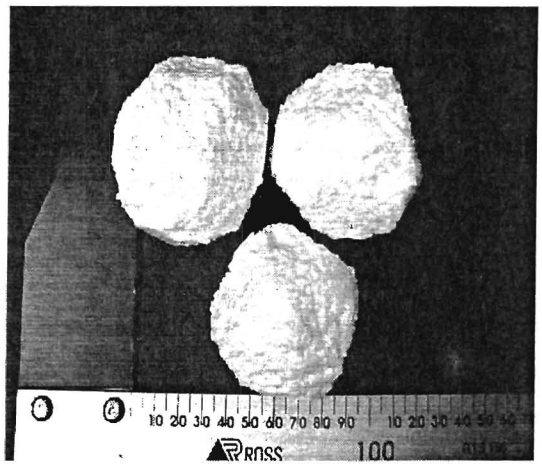

Figure 39: Examples of the polystyrene 'air bubbles' sizes used in the experiments.

The aim of this experiment was to determine what the difference would be when compared to the measurement with 100% air as the dielectric medium. The 'air bubble' was secured in the centre of the vessel and lowered down to a level where the maximum effect could be obtained between the capacitive electrodes, as shown in Figure 40.

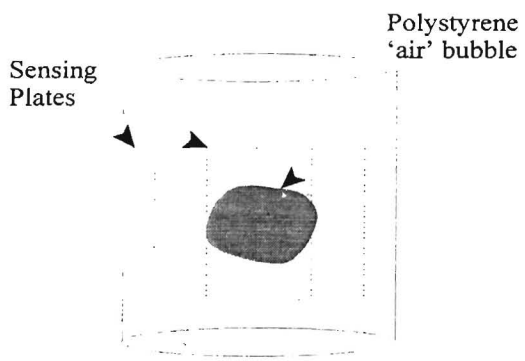

Figure 40: The figure shows the position of the polystyrene bubble in relation to the sensing electrodes.

Figure 41 shows the measurement results obtained when a bubble of polystyrene is placed in the centre of the vessel. From the onset it appears as if the experiment with 100% air and the experiment above provided a similar pattern of results, except for the reading of dielectric reading of 2.56 on the z-axis. To determine whether any meaningful conclusion could be drawn from this experiment it was decided to subtract the two experiments (experiment with air as medium, and experiment with polystyrene and air as medium) from each other, and to use the resultant value as the lower capacitance range. In future experiments when air is simulated by means of a polystyrene bubble, these values will be used as the lower capacitance range.

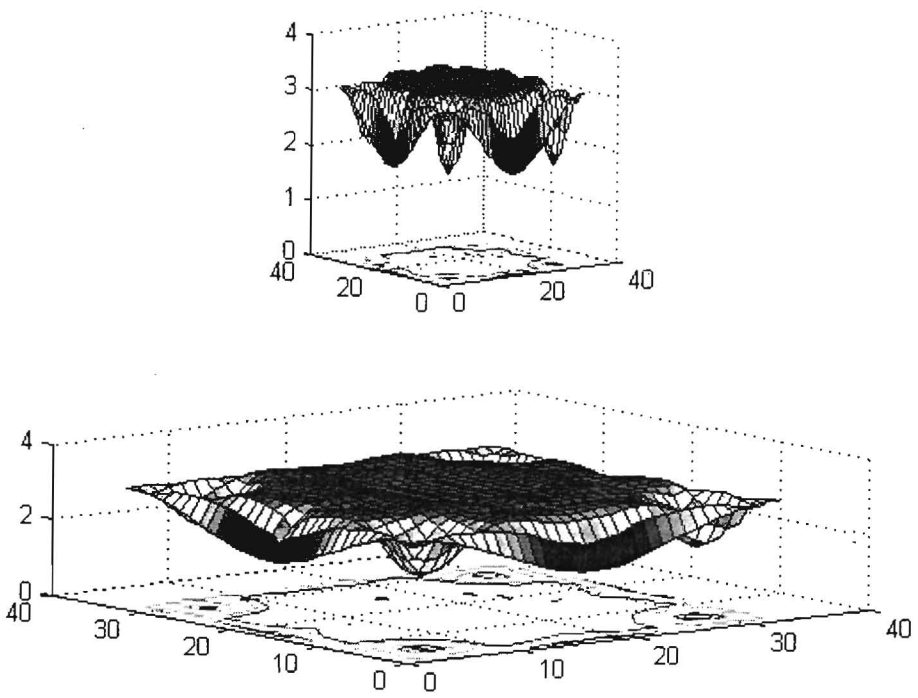

Figure 41: The main plot in the figure shows the flat response of the polystyrene in the centre of our vessel. The slight differences in shading around the centre, when compared to Figure 38, can be contributed to the small difference between the dielectric constant of air and polystyrene. The subplot shows the same results at a different angle.

From the resultant graph in Figure 42, it can be seen that the system one again produced a flat response with notable differences in the shading at the centre of the vessel. The difference in the dielectric constant of air polystyrene is not that significant, although the presence of the polystyrene can be seen by the elevation in the centre of the main plot. In the subplot the resolution and viewing angle has been improved. The variations in the centre of the vessel where the polystyrene is present, can be seen. The resultant value will be used in future experiments where it was found to be less of an effort to insert polystyrene 'air bubbles' into the vessel than small balloons filled with air.

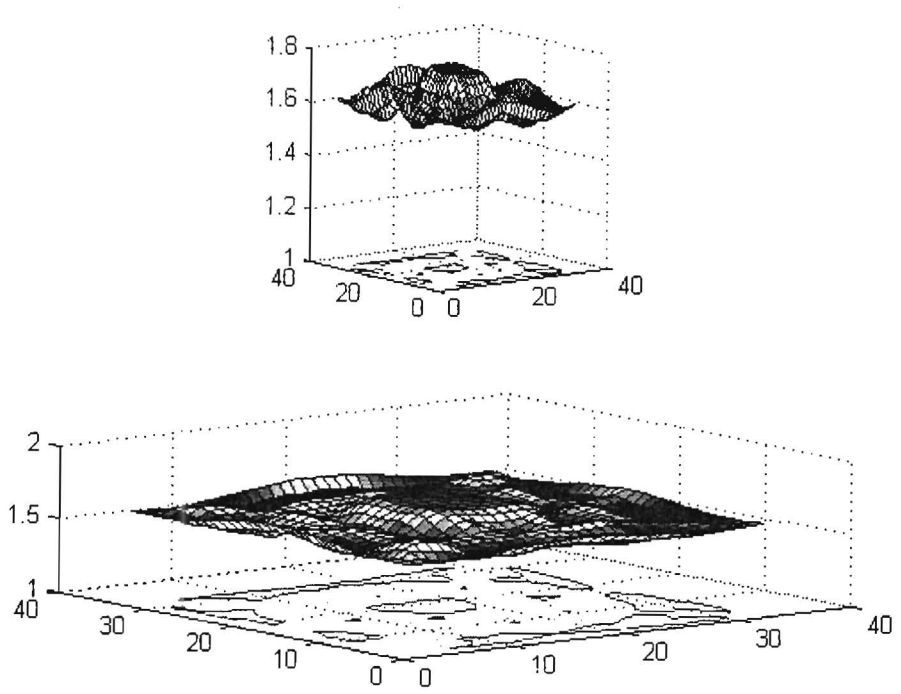

Figure 42: The 3-D surface plot shows the resultant when the data values of the experiment with 100% air, and the experiment with the polystyrene in the centre of the vessel are subtracted. The results show a slight elevation in the centre of the graph where the polystyrene is present. The subplot shows a improved resolution of the results. This resultant value will be used in experiments where polystyrene is used to simulate air bubbles.

6.3 Experiment 3: 100% Sea-Water

The third batch of experiments all included the measurement of different levels of seawater. Firstly, the vessel was filled to capacity with sea-water. This experiment enabled us to determine the upper threshold level of the system. Our water temperature was measured to be 21 °C and from the results in Figure 43, it can be seen that with the dielectric constant of 80.37 for water at 20 °C, and 78.54 for water at 25 °C, the saturated system provided a uniform response over the entire area. The subplot shows larger variations around the perimeter of the vessel which can be ignored. The results of this experiment suggests that our system is able to function without being saturated when filled to capacity with seawater.

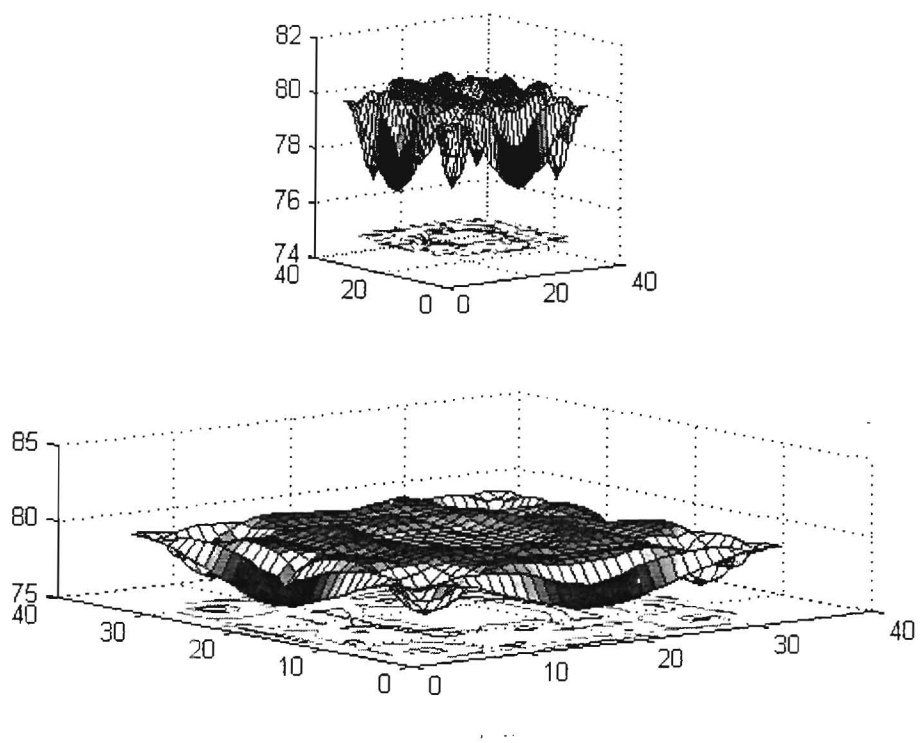

Figure 43: The main plot also shows a flat response over the range, and is centred around the dielectric constant of 80.37 for water. The subplot shows the same results with a improved resolution and view angle.

6.4 Experiment 4: Vessel Filled to 20% Capacity

It was also interesting to determine what the results would be when the vessel was filled with seawater at different levels. The following batch of experiments all refer to Figure 44, showing the results obtained at different voltage levels.

The first experiment was performed by removing 80% of the seawater used in the previous experiment. With the aid of this experiment we were able to determine what the response of the system would be with seawater approaching the level of the sensing electrodes. The results showed an overall increase in the output voltage.

With the water level rising to 20%, and subsequently to near full capacity in the following experiments, a distinct trend is observed whereby the output voltage declines as the distance between the electrodes increases, and visa versa. When progressing along the x-axis it can be seen that the rate of output voltage change shows an upward trend. This phenomenon occurs due to the master electrode and sensing electrode being adjacent or closer to each other as shown previously in Table 1.

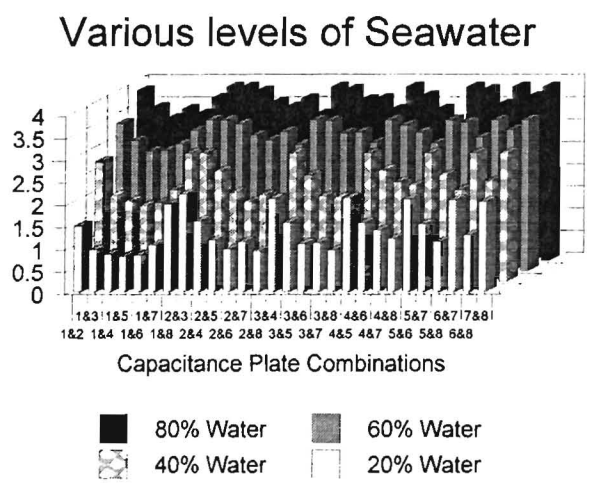

Figure 44: The results show an increase in output voltage as the level of the water rises over the sensing area.

6.5 Experiment 5: Vessel Filled to 40% Capacity

A similar experiment was done by filling the vessel with seawater to 40% of the capacity. The output voltage increased with an average of 1 volt from the previous results. The phenomenon of a higher output voltage with the distance between the driving and sensing electrodes varying, is once again observed.

6.6 Experiment 6: Vessel Filled to 60% Capacity

With the seawater level gradually approaching the maximum point, it can be noted from the graph that the differences between the minimum output voltage and the maximum output voltage has decreased. A clarification for this behaviour would be that the system is approaching the saturation point, as can be seen from the results shown in Figure 44.

6.7 Experiment 7: Vessel Filled to 80% Capacity

From the resultant graph in Figure 44, it can be seen that the measurements taken were nearing the output voltage levels obtained from the system filled to 100% capacity. The system was re-tuned to provide an maximum output voltage of 5 volt when the driving and sensing electrodes were directly adjacent. We would then conclude by deducing that the maximum output voltage we were to measure would be when the vessel was filled to capacity with seawater, and we were only measuring the output voltage with seawater as the dielectric medium. Any other material inserted into the vessel would provide a output voltage in the range of 0-5V.

6.8 Experiment 8: Polystyrene 'Air Bubbles' Vertically Opposite

An experiment was set up by inserting two polystyrene 'air bubbles', similar to those shown in Figure 45, on vertically opposing sides of the vessel as shown below, with the rest of the volume taken up by water.

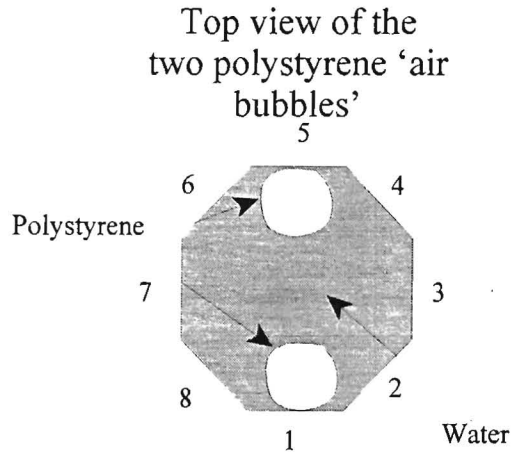

Figure 45: The vertical position of the two polystyrene 'air bubbles' opposite electrodes 1 and 5 are shown.

The experiment was performed to prove whether the directly opposite driving and sensing electrodes 1 and 5, would detect the presence of the bubbles, or if the readings would remain similar to the readings obtained in the previous experiment where the polystyrene was placed in the centre of the vessel. Other conclusions that could be drawn from this experiment would be whether there is a difference between the measurements received from electrode combinations 1,5 and electrodes 3, 7. This would prove that the polystyrene 'air bubbles' placed in close proximity of the driving and sensing electrodes can be detected.

Firstly, the vessel was filled with 100 % seawater and the polystyrene 'air bubbles' placed in position. The 3-D plot shown below is the resultant output voltage of the synchronous detection capacitance sensor, plotted against the 'dielectric weight' distribution of the 80 segments in the octagonal space, when the readings obtained with seawater only are deducted from those obtained with two polystyrene bubbles in vertically opposite positions.

By observing the results in the graph below we can clearly see that the largest difference between the output voltages are obtained when the driving and sensing electrodes are directly opposite each other. Furthermore it can be noted that there is a large variation in the results when measurements are made in the zone between electrodes 1,5 and 3,7 . When measurements are made between these electrodes, the segments closest to the driving and sensing electrodes are segments (33, 42, 43, 59, 60, 74, and 37), as well as (37,50, 51, 67, 68, and 78). These produce the peaks shown on the 3-D surface plot. This suggests that our system is able to detect the presence of the 'air bubbles' in the positions indicated in Figure 46.

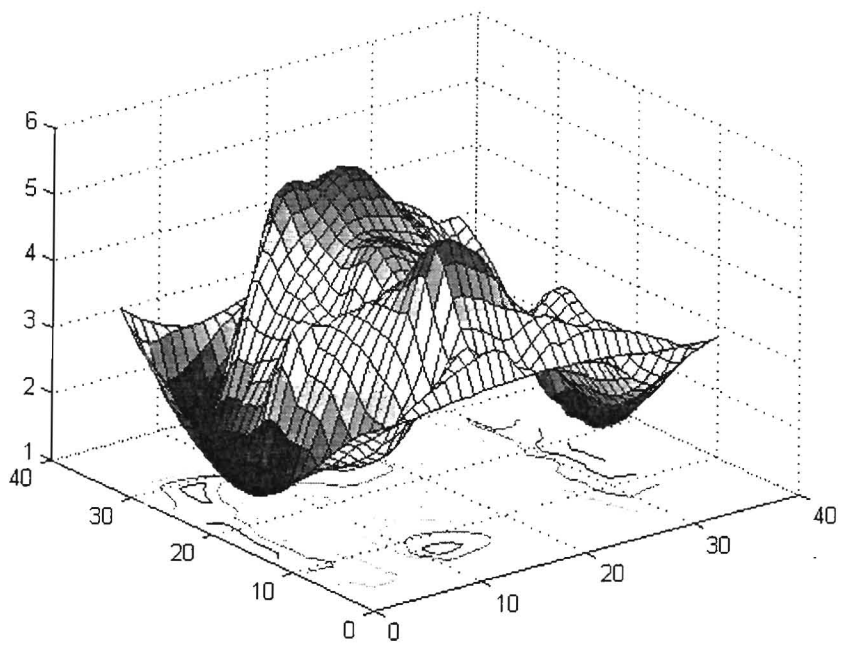

Figure 46: The 3-D surface plot shows the peaks when measurements are made in the zones where the segments (33, 42, 43, 59, 60, 74, and 37, 50, 51, 67, 68, and 78) are closest to the driving and sensing electrodes.

In the following experiment the same polystyrene 'air bubbles' are moved by 90° to the opposite horizontal positions. The aim of this experiment is to determine whether similar results are possible, and to prove beyond doubt that our system is capable of distinguishing between the two positions.

6.9 Experiment 9: Two 'Air Bubbles' Separated Horizontally

In this experiment the same 'air bubbles' were used in opposite horizontal positions. The aim of the experiment was to show that our system is capable of detecting the 'air bubbles' when moved to the horizontal position.

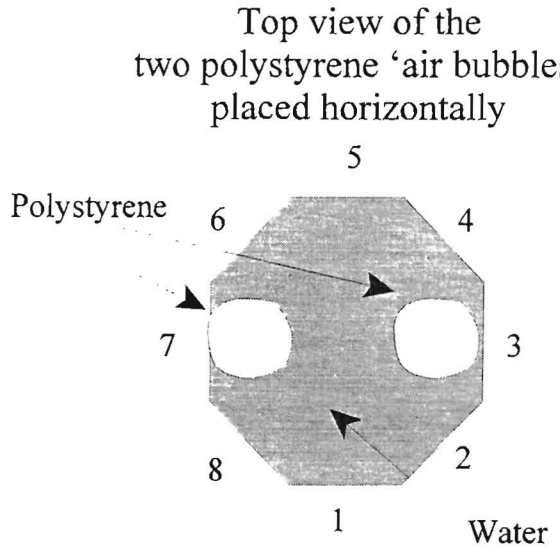

Figure 47: The positions are shown with the 'air bubbles' adjacent to electrodes 3 and 7.

The results in Figure 45 exhibit a definite difference in the resultant output voltage when plotted against the dielectric weight distribution of each segment in the octagonal area. The largest differences occur in the zone when the driving electrode (electrode 3), and the sensing electrode (electrode 7) are directly opposite each other. The segments that are most affected in this case are segments 39, 54, 55, 71, 71, and 80, as well as, 35, 63, 64, and 76. Other peaks indicating a larger difference in output voltage also occur when electrode 3 is the driving electrode. This, we assume, is due to the attenuation effect the polystyrene 'air bubble' has on the driving electrode (3) signal and the receiving electrode (7) reception. This once again proves that the 'air bubble' is definitely detected by our system whether it is in the vertically or horizontally opposing positions.

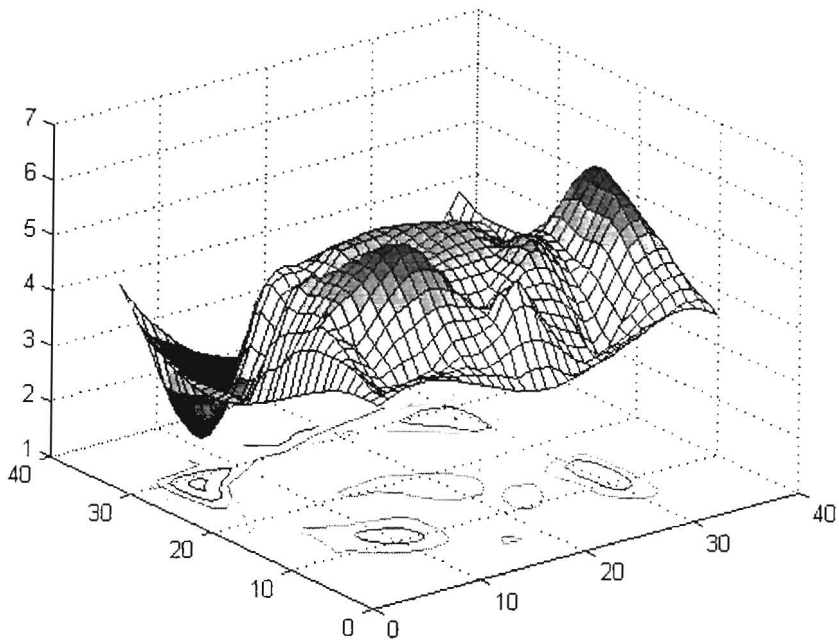

Figure 48: It can be seen from the figure that the peaks on the surface and the contour plots now occur when the segments that are most affected in this case, are close to the sensing and driving electrodes.

6.10 Experiment 10: Vessel Filled with a Gravel Lump in Centre

In the following experiment gravel was suspended into the centre of the vessel filled with seawater. The experiment would show what reaction our system would have when gravel chips and seawater are combined, are placed in the centre of the vessel, to form the dielectric medium.

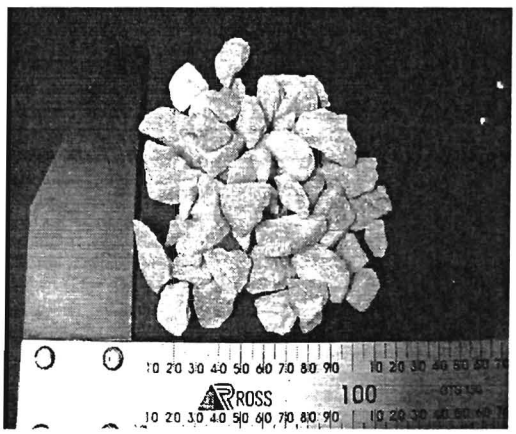

Figure 49: The photograph shows the size of the gravel chips used in the experiments.

The size of the gravel chips used in all experiments are indicated in Figure 49. A stocking filled with the 500 g of gravel chips was suspended into the vessel at the position shown in Figure 50.

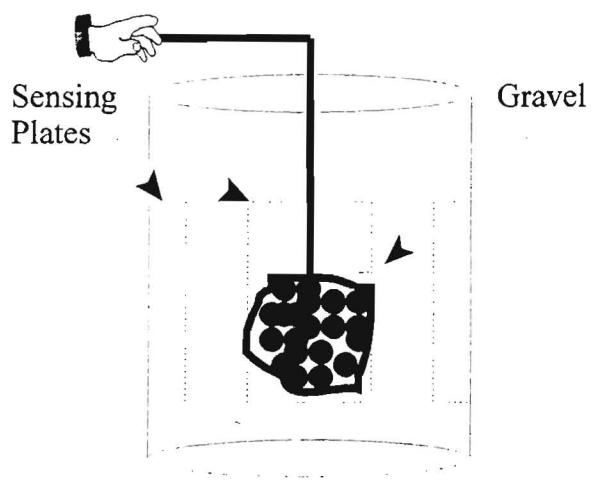

Figure 50: The gravel chips were suspended into the centre of the vessel, and placed across the sensing area of the electrodes.

Thereafter, the measurements taken in the experiment with 100% seawater alone, were compared to this experiment, to determine what effect this change in dielectric properties would have on the system. It must be emphasised that the aim of this experiment was not to determine what the size or shape of the introduced medium (gravel) was, but to prove that there was a difference in diagonal readings when compared to the experiment with 100% seawater. By making use of the results obtained for 100% seawater, and plotting this against the results of those obtained when gravel is inserted into the centre, we could prove that the system is able to detect the presence of the gravel by only using the diagonal measurements, as shown in Figure 51.

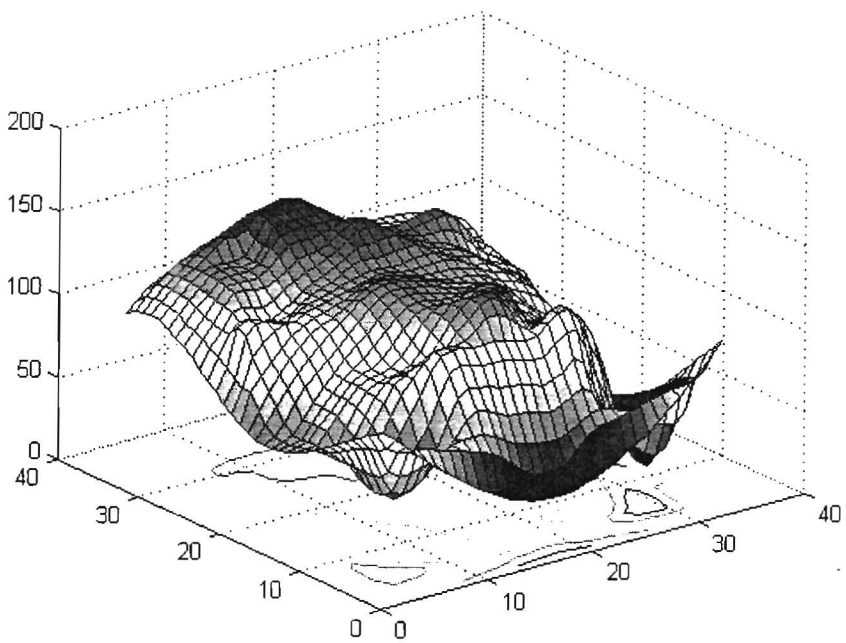

Figure 51: The 3-D plot shows the dielectric distribution of the gravel chips placed in the centre of the vessel. The pronounced peaks noted when the 'air bubbles' were placed in the vessel are not that obvious, and could be attributed to the smaller difference in dielectric constants of water and gravel.

From the results it can be seen that the maximum difference between the results for the experiment with 100% seawater, and these taken with the gravel in the centre, occur when the driving and sensing electrodes are diagonally across each other.

6.11 Experiment 11: Two Gravel Masses Separated Vertically

The an experiment was set up by suspending two gravel masses of 250g each, on opposing sides of the vessel, as shown in Figure 52.

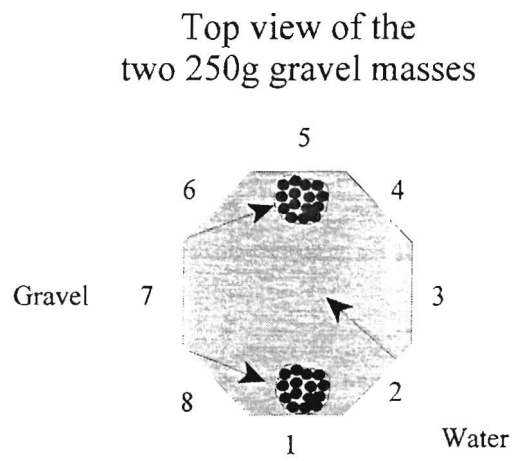

Figure 52: The figure shows the vertical positions of the two gravel masses. The sensing and driving electrodes 1 and 5 are most affected in this configuration.

The experiment was performed to prove whether the adjacent driving and sensing electrodes, 1,2; 1,8; 4,5; and 5,6 would detect the presence of the gravel, and what effect the gravel has on electrodes 1 and 5.

Other conclusions that could be drawn from this experiment would be:

l) Whether the measurement between electrodes 3 and 7 differ from the measurements between electrodes 1 and 5?

m) How much effect does the close location of the gravel masses have on the driving and sensing sensitivity of say, electrodes 1 and 5?

Once again the measurements taken with pure seawater was weighted against the results obtained by suspending the two vertically opposite masses of gravel into the seawater. By observing the results in the graph below we can clearly see that the largest difference between the output voltages are obtained when the driving and sensing electrodes are directly opposite each other. Further it can be noted that there is a large variation in output voltages when measurements are made between electrodes 1,5 and 3,7. We assume that the smaller peak on the one side of the 3-D plot can be attributed the fact that the sensing signal has been attenuated severely by the presence of the gravel lump at the sensing electrode. What we have shown is that our system is sensitive to the presence of gravel masses in the vertical position.

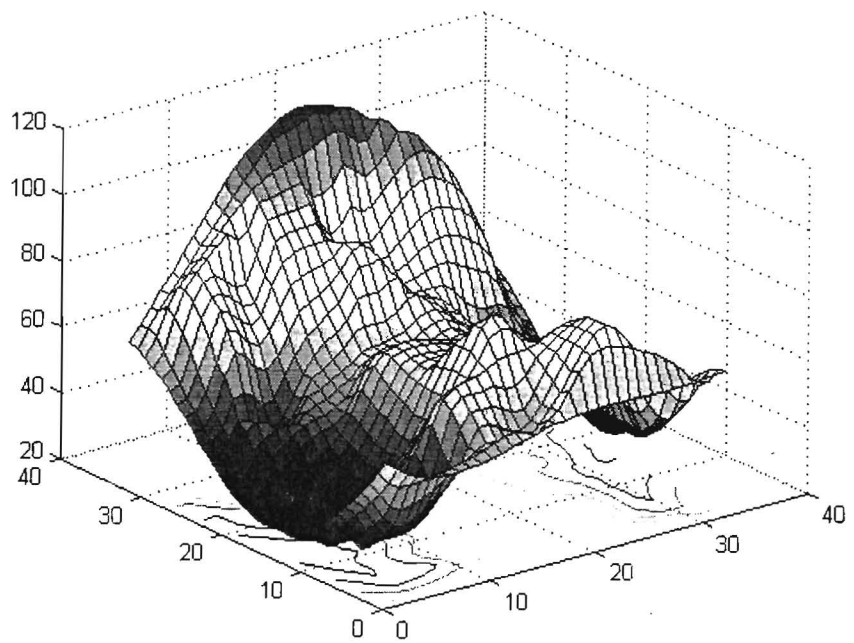

Figure 53: From the 3-D plot it can be seen that a large peak occurs at the one end of the vessel. This can be attributed to the fact that the signal received at the sensing electrode has been attenuated by the gravel lump closest to the sensing electrode.

In the following experiment the same gravel masses are moved by 90° to the opposite horizontal position. The aim of this experiment is to determine whether similar results are possible, and to prove beyond doubt that our system is capable of distinguishing between the two positions.

6.12 Experiment 12: Two Gravel Masses Separated Horizontally

In this experiment the same gravel masses were used in opposite horizontal positions. The aim of the experiment was to determine if our system is capable of detecting the masses now moved to the horizontal position as shown in Figure 54.

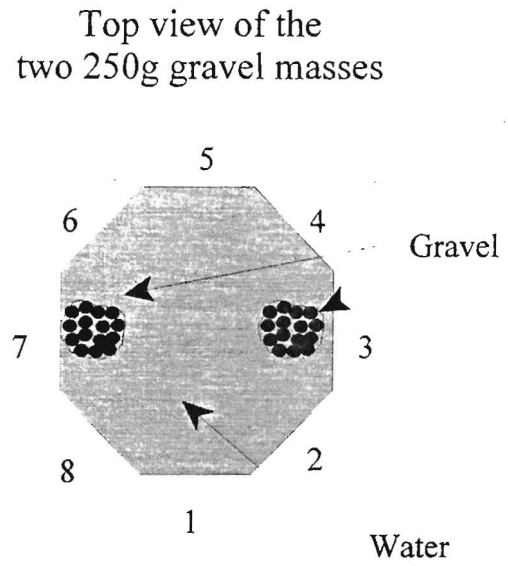

Figure 54: The figure shows the two 250g gravel masses positioned horizontally.

The results in Figure 55 show a movement in the sensing data towards electrode 7. An assumption can be made that the peak not detected on the opposite electrode 3, is due to the attenuation affect of the gravel on the sensing electrode. The aim was to show that the measurements differed when compared to those taken in the vertical position. This was achieved, and further refinement is needed on the system to clearly distinguish between the presence of gravel in the vertical and horizontal positions.

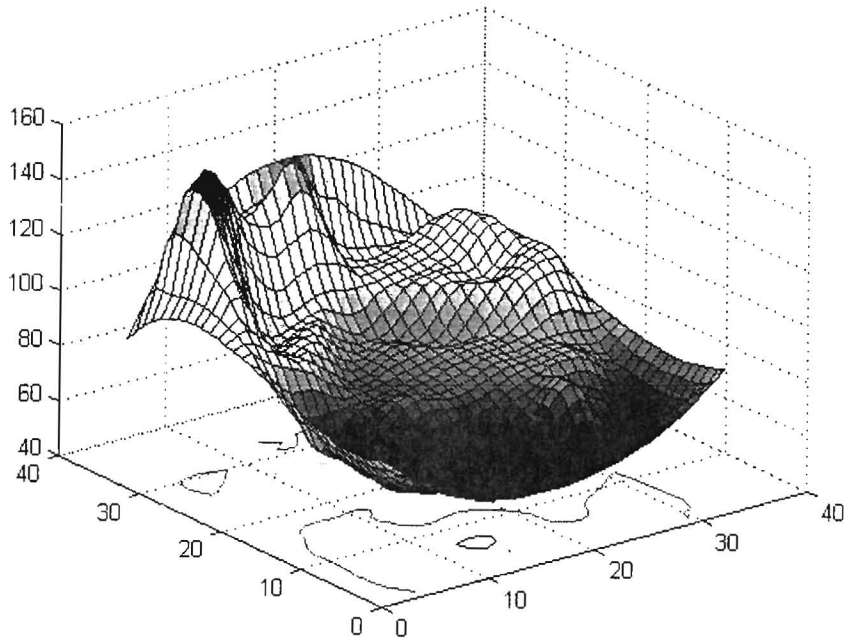

Figure 55: The 3-D figure shows the detection of the gravel lump at a new position. Once again the presence of the opposite peak is not detected, and it is assumed that attenuation of the sensing signal has occurred.

6.13 Experiment 13: Gravel Mass and 'Air Bubble' Directly Opposite

From our previous experiments with gravel and air (simulated by polystyrene) it is evident that our system can detect the difference between only air, or only gravel inserted into the vessel. We also noted a variation when the gravel masses and 'air' bubbles were moved to different positions in the vessel. In this experiment we placed one 250g mass of gravel, and one polystyrene 'air' bubble at the positions shown in Figure 56.

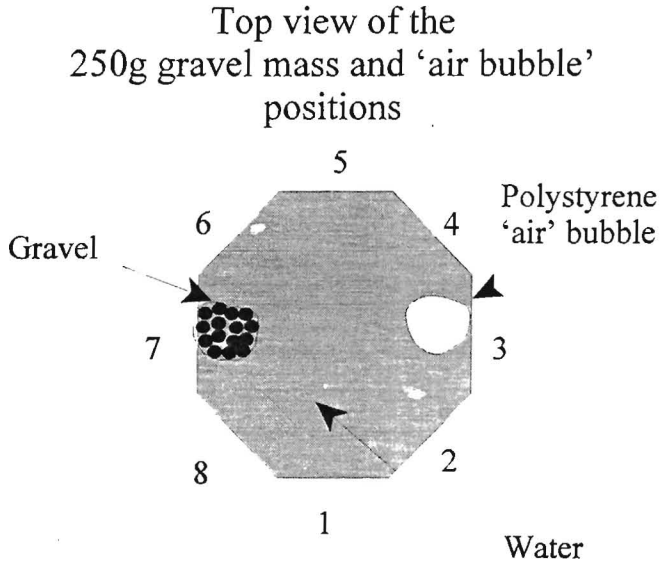

Figure 55: The figure shows the positions of the 'air bubble' and 250g gravel mass for the current experiment.

From our results we expected two different peak areas with the different materials at the face of the driving and detecting electrodes. With the 28 independent measurements starting with capacitance electrode 1 as the master driving electrode, and rotating anti-clockwise until electrode 7 is the master electrode, it can be seen that the 'air bubble' will not be adjacent to the driving electrode when the measurement between electrode 7 and 8 are made, as shown in Figure 57.

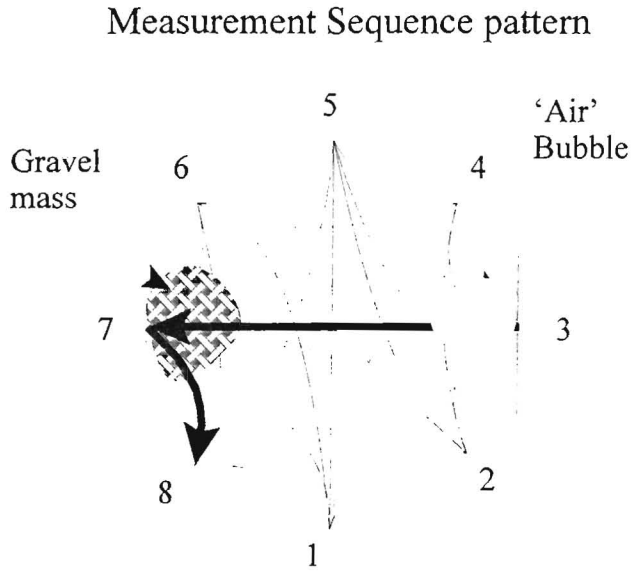

Figure 57: The 28 measurement sequences from electrode 3 to 7 , and from electrode 7 to 8, together with the gravel and 'air bubble' positions are shown.

Likewise, when the measurement between electrodes 3 and 7 are made, the driving electrode (3) is obstructed with the 'air bubble', and the receiving electrode (7) is partly hidden behind the gravel mass, as shown in Figure 57.

In this experiment, we expect the peak at the 'gravel electrode' to be different to the peak at the 'air bubble' electrode. Figure 58 shows the results obtained from the experiment when the gravel and 'air bubble' were positioned horizontally. From the 3-dimensional plot the results show a marked difference between the two horizontally opposite peaks. We also expect that, when the 'air bubble' and gravel samples are switched, the output voltage would decline when the driving electrode (3) has the gravel as an obstacle.

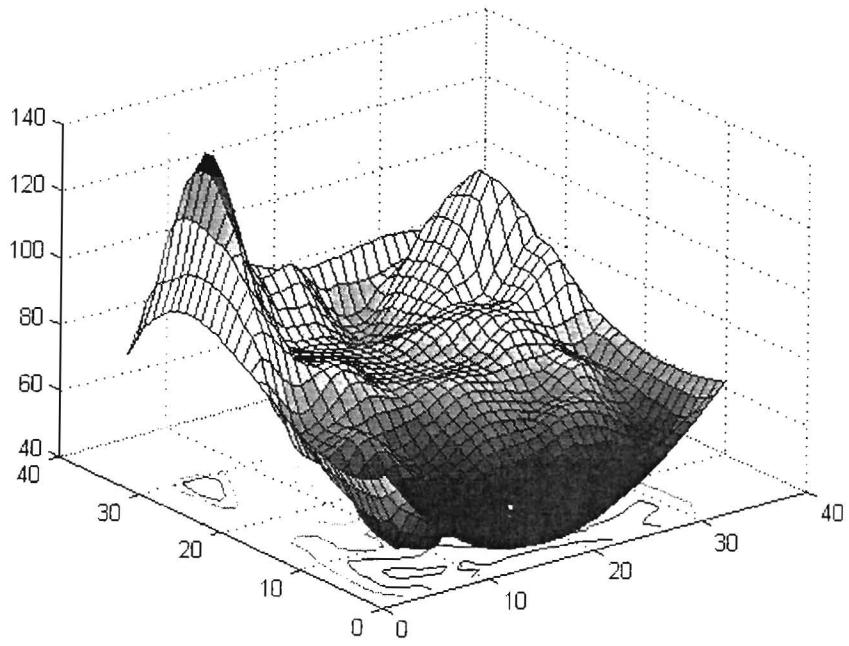

Figure 58: The horizontal position of the 250g gravel mass in relation to the 'air bubble' on the opposite side can be seen.

Another interesting factor to note is the higher output voltage differences would be present towards the latter stages when electrode 6 and 7 are the driving electrodes. It could be expected that the differences would be are higher when the 'air bubble' is at the driving electrode than when compared to the results with the gravel adjacent to the driving electrode.

Our future work will include neural networks to discriminate between the different materials. Our aim, as mentioned earlier, is to detect a difference in output voltage with various combinations and positions of gravel and 'air bubbles' in our vessel.

6.14 Experiment 14: Smaller Gravel Masses and 'Air Bubbles' in the Centre

The aim of this experiment is to determine what the effect on the system would be when a combination of 'air bubbles' and gravel samples were placed in the centre of the vessel. It was not aimed at distinguishing between the various combinations, as this would require the use of advanced algorithms and neural networks, but to determine whether the system would saturate.

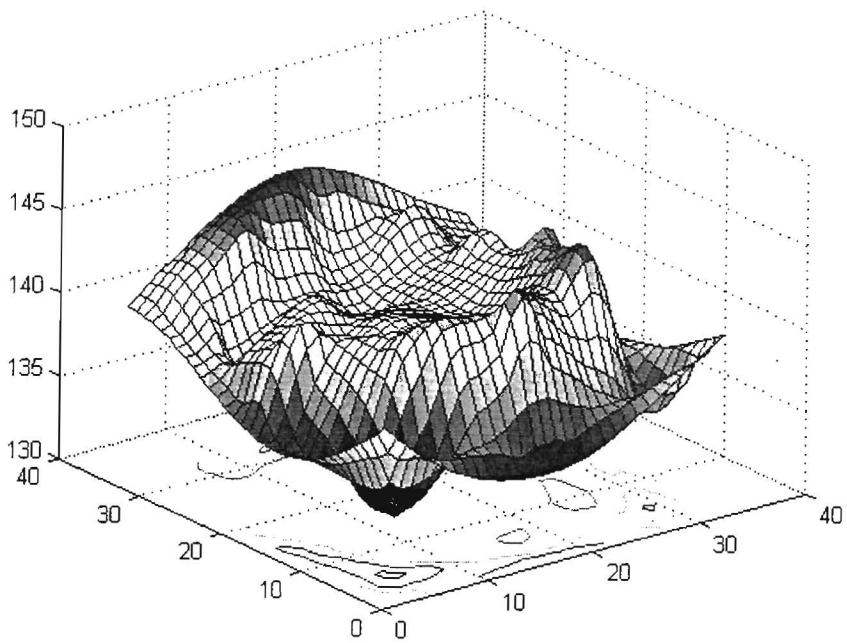

Figure 59: The 3-D surface plot shows a concentration of dielectric distributions around the centre of the vessel, indicating the ability of our system to detect the presence of gravel and 'air bubbles'.

The results in Figure 59 show various smaller peaks around the centre of the vessel. This proves that a combination of 'air bubbles' and gravel could also be detected. It must however be stated that in order to discriminated between the volumes of 'air' and gravel, the system would require the implementation of artificial intelligence in the form of a neural network. Another very important fact that we noticed was that the system did not saturate, and that the maximum and minimum points in equivalent voltage variations were are approximately 1 volt. This can be seen in Figure 60, where the voltages obtained from the capacitance/voltage conversion process are plotted.

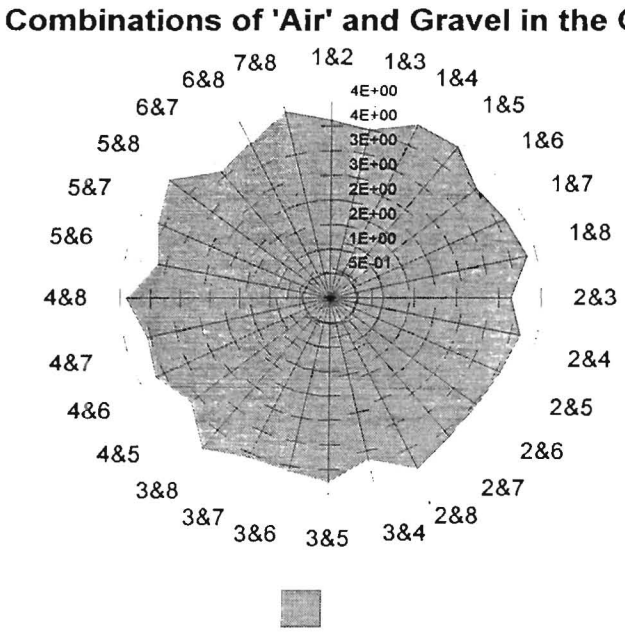

Figure 60: The graph show the results when various combinations of 'air bubbles' and gravel are placed in the centre of the vessel. The radial axis is the output voltage range from 0-5V.

Chapter 7:

Conclusions and Recommendations

This project has investigated the feasibility of using capacitance tomography techniques to identify the phase components of multi-phase material. The self-tuning capacitance techniques used were found to be repeatable and accurate. Variations in the output voltage of the self-tuning synchronous detection measuring instrument were evident when materials and combinations of materials were sensed. A capacitance tomographic measurement was achieved using a multiple electrode array mounted around the exterior of a vessel (pipe).

A multiplexer and digital interface system was used to obtain a sequence of capacitance measurements within the tomography vessel. The resulting sequence of capacitance measurements was then used as a basis for determining whether the presence of multi-phase components could be detected. These voltage levels as such form a complex array of measurements which are dependent on material content, measurement area, and the geometry. A simple approach using a graphical transformation, and an interpolation into a three dimensional contour/surface graph by means of Matlab, was used. This technique can be viewed as a simplistic neural network, however, the training and optimisation of this system into a discretionary system, is left as a future development.

From the results of simulated multiple-phase conditions, it was shown that the three dimensional graphs are visually distinctive and represent a qualitative measurement of the physical configuration. The material content and distribution could to a large extent be determined from the measured dielectric value (as represented on the graph). However, some confusion exists when viewing the graph plots resulting from combinations of materials that have been inserted in the vessel. In this more complex configuration a more advanced discretionary system would be required to extrapolate the material content of the vessel. Although this is left to future work, the existing system has been able to detect multi-phase materials with diverse dielectric properties in the presence of an extremely saline medium. This is encouraging and it is therefore possible to extended this work to a full dynamic capacitance tomography system with a more advanced

discretionary component.

7.1 Future work

The system was not able to discriminate clearly between more than two material phases, when combinations were tested, but was able to individually detect the presence of air and gravel placed at different positions. This is not necessarily a shortcoming of the sensor system but rather a shortcoming of the discrimination approach used. Future work would require that a more advanced artificial intelligence system, possibly in the form of a neural network, and/or image reconstruction algorithms which make use of the back-projection method (as described by Huang *et al* [9]) be used to obtain the flow image. Image reconstruction algorithms would have to take into account the field distortion caused by high loss or high permittivity components (eg saline water). It is also possible that some applications would require a dual modality tomography system comprising capacitance and resistance measurements. A feature of the capacitance sensor system presented in this work is that conductance and capacitance are measured simultaneously. Therefore the system could readily be extended to meet this need (if required).

Future work aimed at a system capable of resolving multiple phase flow within pipes would also have to take into account the dynamic nature of the measurement and the process itself. This process would firstly require a detailed understanding of the dynamic characteristics of the capacitance sensor system (settling time and switching time required to complete a measurement sequence). Secondly, the dynamic nature of the flow itself would have to be considered (hydro-mechanics).

This work can be used as the basis for the aforementioned developments.

REFERENCES

[1] M Beck, R Williams, "Process Tomography: a European innovation and its applications", *Meas. Sci. Technol*, vol. 7, pp. 215-224, 1996.

[2] M S Beck and A Plaskowski, "Cross Correlation Flowmeters - Their Design and Application", *(Bristol: Adam Hilger)*, 1987.

[3] R He, C M Beck, R C Waterfall, and M S Beck, "Applying capacitance tomography to combustion phenomena", *Proc. European Concerted Action on Process Tomography, Karlsruhe*, pp. 300-302, 1993.

[4] R He, C M Beck, R C Waterfall, and M S Beck, "Development of capacitance measurement towards tomographic imaging of flames", *IOP'93 Sensors & Their Applications*, (Bristol: IOP), 1993.

[5] G A Johansen, T Froystein, B T Hjertaker, O Isaksen, O Olsen, S K Strandos, T S Olsen, E Abro, B McKibben, S Heggstad, and E A Hammer "The design of a dual mode tomograph for three-component flow imaging", *Proc. European Concerted Action on Process Tomography, Oporto,* pp. 75-80, 1994.

[6] C G Xie, A Plaskowski, and M S Beck, "8-Electrode capacitance system for two-component flow identification, part 1: tomographic flow imaging", *IEEE Proc.* vol. A136, pp. 173-183, 1998.

[7] C G Xie, A Plaskowski, M S Beck, "8-Electrode capacitance system for two-component flow identification, part 2: tomographic flow imaging", *IEEE Proc.* vol. A136, pp. 184-190, 1998.

[8] C G Xie, A Plaskowski, M S Beck, "Design of capacitance electrodes for concentration measurement of two-phase flow", *Meas. Sci. Technol.* vol. 1, pp. 65-78, 1990.

[9] S M Huang, A Plaskowski, C G Xie, and M S Beck, "Capacitance-based tomographic flow imaging system", *Electron. Lett.* vol. 24, pp. 418-419, 1988.

[10] S M Huang, A Plaskowski, C G Xie, and M S Beck, "Tomographic imaging of two-phase flow using capacitance sensors", *J. Phys. E: Sci. Instrum.*, vol. 22, pp. 173-177, 1988.

[11] N Reinecke, and D Mewes, "Resolution enhancement for multi-electrode capacitance sensors", *Proc. European Concerted Action on Process Tomography, Oporto,* pp. 50-61, 1994.

[12] Klug F and Mayinger F, "Novel impedance measuring technique for flow composition in multi-phase flows", *Proc. European Concerted Action on Process Tomography, Karlrushe*, pp. 152-5, 1993.

[13] Huang S M, Plaskowski A, Xie C G, and Beck M S, "Tomographic imaging of two phase flow using capacitance sensors", *J. Phys. E: Sci. Instrum.* vol 22, pp. 173-7, 1989.

[14] Endress and Hauser patent 84087 on a capacitance comparator measuring circuit, 1984.

[15] S M Huang, A Plaskowski, G Green, and M S Beck, "A high frequency stray-immune capacitance transducer based on the charge transfer principle", *IEEE Trans. Instrum.* , vol. 3, pp. 368-373, 1988.

[16] F Dicken, M Wang, "Electrical resistance tomography for process applications", *Meas. Sci. Technol*, vol. 7, pp. 247-260, 1996.

[17] M Z Abdullah, "Electrical impedance tomography for imaging conducting mixtures in hydrocyclone separators", *PhD Thesis*, UMIST, 1993.

[18] P Hua, E J Woo, J G Webster, and W J Tompkins "Using compound electrodes in electrical impedance tomography", *IEEE Trans. Biomed.* vol 40, pp. 29-34, 1993.

[19] M Wang, "Electrical impedance tomography on conducting walled vessels", *PhD Thesis*, UMIST, 1994.

[20] K C Tanner, "The development of a dielectric approach to oil condition assessment", *BTech Thesis*, Cape Technikon, 1996.

[21] D Marioli, E Sardini, A Taroni, "High-accuracy measurement techniques for capacitance transducers", *Meas. Sci. Technol.*, vol. 4, pp. 337-343, 1993.

[22] Q Smit, B J P Mortimer, J Tapson, "General Purpose Self-tuning Capacitance Sensor", *MTech Thesis*, Cape Technikon, 1998.

[23] M S Beck, A Plaskowski, "How inherent flow noise can be used to measure the mass flow of granular materials", *Instrum. Rev.*, 1967.

[24] C G Kozubowski, "*Korrelacjonnyje Ekstremalnyje Sistiemy*" (Kijew: Naukowa Dumka), 1973.

[25] W Balachandran, "Measurement of suspended solids concentration and volumetric flows of slurries and sludges", *PhD Thesis*, University of Bradford, 1979.

[26] K Komiya, "Flow velocity measurement using cross correlation techniques", *Bulletin National Research Lab of Metrology, Tokyo* , series 12, pp. 64-72, 1986.

[27] J S Battye, "An industrial correlation flowmeter", *PhD Thesis*, University of Bradford, 1976.

[28] J Coulthard, "Flow measurement by cross correlation of ultrasonic waves", *PhD Thesis*, University of Bradford, 1973.

[29] C Wormald, "Fluid flow measurement by non-contacting methods", *PhD Thesis*, University of Bradford, 1973.

[30] K H Ong, "Hydraulic flow measurement using ultrasonic transducers and correlation techniques", *PhD Thesis*, University of Bradford, 1975.

[31] E A Hammer, "Three-component flow measurement in oil/gas/water mixtures using capacitance transducers", *PhD Thesis*, University of Manchester, 1983.

[32] E Dykesteen, A Hallanger, E A Hammer, E Samnoy, and R Thorn, "Three-Component Flow Measurement. The Admittance Method-Basic Principles", *Report No 4, CMI Norway* , vol. 831251-1, 1983.

[33] L-A Xu, *PhD Thesis* University of Manchester, 1986.

[34] T Hargitai, D Horanyi, D Pallagi, and S Tozser, "Microprocessor based multichannel polarity cross correlator for flow rate measurement", *Proc. FLOMEKO Conf. (Budapest)*, pp. 117-124, 1983.

[35] M S Beck and A Plaskowski, "Cross Correlation Flowmeters - Their Design and Application", pp. 11-13, *(Bristol: Adam Hilger)*, 1987.

[36] J A Nuijten, R P Keech, and J Coulthard, "Industrial mass flow measurement trials using an ultrasonic cross correlation flowmeter", *Proc. FLOMEKO Conf. (Budapest)*, 1983.

[37] M S Beck and A Plaskowski, "Cross Correlation Flowmeters - Their Design and Application", pp. 61-74, *(Bristol: Adam Hilger)*, 1987.

[38] M S Beck and A Plaskowski, "Cross Correlation Flowmeters - Their Design and Application", pp. 75-80, *(Bristol: Adam Hilger)*, 1987.

[39] A L Stott, R Green, K Seraji, "Comparison of the use of internal electrodes of the measurement of capacitance and conductance of fluids in pipes", *J. Phys. E: Sci. Instrum.* vol. 18, 1985.

[40] E A Hammer, "Three-component flow measurement in oil/gas/water mixtures using capacitance transducers", *PhD Thesis*, University of Manchester, 1983.

[41] WWW, URL "http://www.neusciences.com/nn_spvs2.htm", 1999.

[42] N Ampazis, "Introduction to Neural Networks", http//www.iit.demokritos.gr/neural/intro/, 1999.

[43] D E Rumelhart, G E Hinton, and R J Williams, "Learning representations by back-propagating errors", *Nature, 323*, pp. 533-536, 1986.

[44] D E Rumelhart and R McClelland, "Parallel Distributed Processing: Explorations in the Microstructures of Cognition", *Nature, 323*, pp 587-589, 1986.

[45] CRC Handbook of Chemistry and Physics, 58th Edition, pp. E55-61, 1977-1998,

[46] CRC Handbook of Chemistry and Physics, 58th Edition, pp. E59-60, 1977-1998,

[48] M.S. Beck, T. Dyakowski, R.A. Williams, "Process tomography - the state of the art", *Trans Inst MC*, Vol 20, No 4, pp. 169-170, 1998.

[49] C.G. Xie, S.M. Huang, B.S. Hoyle, R. Thorn, C. Lenn, D. Snowden, and M.S. Beck, "Electrical capacitance tomography for flow imaging: system model for development of image reconstruction algorithms and design of primary sensors", *IEE Proc.-G*, 139, pp. 89-98, 1992.

APPENDICES

APPENDIX A

Matlab Code for 3-D Graphs

```
fid=fopen('c:\matlab\bin\mattom.txt')          %Open the text file with the 28x80 matrix of areas
z=fscanf(fid,'%lf',[28,80])                    %Scan in the whole file 28 col x 80 rows
status = fseek(fid,0,'bof')                    %Set the offset to column 1 beginning of file
a=fscanf(fid,'%lf',[28,80])                    %Scan in all the data. [matlab scans it in as rows by rows
]
w=a'                                           %Transpose the matrix to 28 col x 80 rows
b=ones(80,1)                                   %set up a 1 col matrix with ones
d=80.37                                        %multiply to get the e of the substance (water)
e=d.*b                                         %this is the 1 col with 80 e values in
mm=dlmread('c:\matlab\bin\filename.txt','\t',0,0)   %Read in the ASCII delimited data file
m=mm'                                          %with all the capacitance values
E=(w*m)                                        %Multiply the w matrix(areas) with the capacitance values
k=E.\e                                         %This results it the constant k
ee=(k.*E)                                      %This is the z-plane of data to be plotted in 3-D
xy=[0 -1                                       %The x,y axis for the grid is set up
 1 -1
 1 0
 1 1
 0 1
 -1 1
 -1 0
 -1 -1
 0 -2
 1.5 -1.5
 2 0
 1.5 1.5
 0 2
```

-1.5 1.5

-2 0

-1.5 -1.5

-0.5 -2.5

0.5 -2.5

1.5 2.5

2.5 -1.5

2.5 -0.5

2.5 0.5

2.5 1.5

1.5 2.5

0.5 2.5

-0.5 2.5

-1.5 2.5

-2.5 1.5

-2.5 0.5

-2.5 -0.5

-2.5 -1.5

-1.5 -2.5

0 -3

2.2 -2.2

3 0

2.2 2.2

0 3

-2.2 2.2

-3 0

-2.2 -2.2

-1.6 -3.5

-1.2 -3.5

1.2 -3.5

1.6 -3.5

3.5 -1.6

3.5 -1.2

3.5 1.2

3.5 1.6

1.6 3.5

1.2 3.5

-1.2 3.5

-1.6 3.5

-3.5 1.6

-3.5 1.2

-3.5 -1.2

-3.5 -1.6

-3 -2

-2 -3

-0.5 -3.5

0.5 -3.5

2 -3

3 -2

3.5 -0.5

3.5 0.5

3 2

2 3

0.5 3.5

-0.5 3.5

-2 3

-3 2

-3.5 0.5

-3.5 -0.5

-3 -3

0 -4

3 -3

```
  4 0
  3 3
  0 4
  -3 3
  -4 0]
xyz=[xy ee]                    %Create a new matrix with the x,y, and Z data
em=mean(e)                     %Get the mean of the ee matrix to eliminate all the zero entries
xyz ex=[4 4 em                 %Get rid of all the zero entries
  -4 4 em
  -4 -4 em
  4 -4 em]
xyz=[xyz                       %Set up a new x,y,and z data matrix
  xyzex]
X=xyz(:,1)                     %Column 1 is the X data
Y=xyz(:,2)                     %Column 2 is the Y data
ee=xyz(:,3)                    %Column 3 is the Z data
xi=[-4 -3.75 -3.5 -3.25 -3 -2.75 -2.5 -2.25 -2 -1.75 -1.5 -1.25 -1 -0.75 -.5  -.25 0 0.25 .5 .75 1
1.25 1.5 1.75 2 2.25 2.5 2.75 3 3.25 3.5 3.75 4 ]
yi=[4
  3.75
  3.5
  3.25
    3
  2.75
  2.5
  2.25
  2
  1.75
  1.5
  1.25
  1
```

```
 0.75
 0.5
 0.25
 0
 -0.25
 -0.5
 -0.75
 -1
 -1.25
 -1.5
 -1.75
 -2
 -2.25
 -2.5
 -2.75
 -3
 -3.25
 -3.5
 -3.75
 -4]
[ZI] = griddata(X,Y,ee,xi,yi,'cubic')      %Create the 3-D plot with all the predefined data
surfc(ZI)                                  %Plot the surface in 3-D with the contours included
```

APPENDIX B

APPENDIX C